Cell

Mechanism of CFTR correction by type I folding correctors

Graphical abstract

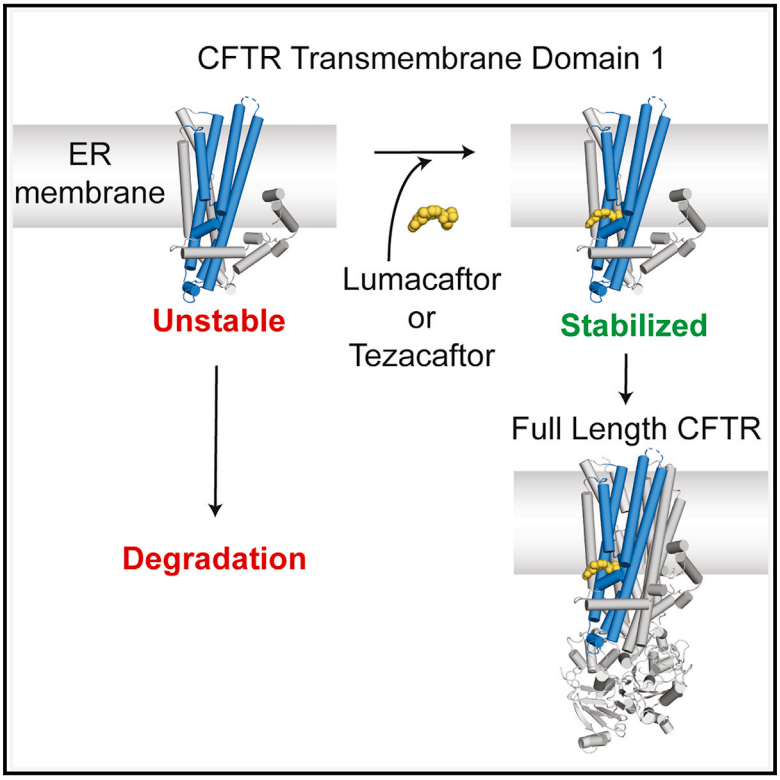

Authors

Karol Fiedorczuk, Jue Chen

Correspondence

juechen@rockefeller.edu

In brief

Drugs used to treat cystic fibrosis act via stabilization of a single domain within CFTR that promotes global folding.

Highlights

- Lumacaftor binds to CFTR in two confirmations
- Tezacaftor and lumacafor bind to the same site on TMD1
- Type 1 correctors stabilize CFTR by filling an internal cavity

Fiedorczuk & Chen, 2022, Cell *185*, 158–168
January 6, 2022 © 2021 The Author(s). Published by Elsevier Inc.
https://doi.org/10.1016/j.cell.2021.12.009

CellPress

CellPress
OPEN ACCESS

Cell

Article

Mechanism of CFTR correction by type I folding correctors

Karol Fiedorczuk[1] and Jue Chen[1,2,3,*]
[1]Laboratory of Membrane Biology and Biophysics, The Rockefeller University, New York, NY 10065, USA
[2]Howard Hughes Medical Institute, Chevy Chase, MD 20815, USA
[3]Lead contact
*Correspondence: juechen@rockefeller.edu
https://doi.org/10.1016/j.cell.2021.12.009

SUMMARY

Small molecule chaperones have been exploited as therapeutics for the hundreds of diseases caused by protein misfolding. The most successful examples are the CFTR correctors, which transformed cystic fibrosis therapy. These molecules revert folding defects of the ΔF508 mutant and are widely used to treat patients. To investigate the molecular mechanism of their action, we determined cryo-electron microscopy structures of CFTR in complex with the FDA-approved correctors lumacaftor or tezacaftor. Both drugs insert into a hydrophobic pocket in the first transmembrane domain (TMD1), linking together four helices that are thermodynamically unstable. Mutating residues at the binding site rendered ΔF508-CFTR insensitive to lumacaftor and tezacaftor, underscoring the functional significance of the structural discovery. These results support a mechanism in which the correctors stabilize TMD1 at an early stage of biogenesis, prevent its premature degradation, and thereby allosterically rescuing many disease-causing mutations.

INTRODUCTION

Cystic fibrosis is a genetic disease caused by mutations in the cystic fibrosis transmembrane conductance regulator (CFTR), an anion channel that regulates salt, fluid, and pH balance in many organs (Cutting, 2015). CFTR belongs to the ATP-binding cassette (ABC) transporter family. It is a single polypeptide composed of two pseudo-symmetrical halves connected by a regulatory domain (RD). Each half of CFTR contains a transmembrane domain (TMD) that forms the ion conduction pathway and a cytoplasmic nucleotide-binding domain (NBD) that binds ATP. The RD, unique in CFTR, must be phosphorylated for the channel to open (Cheng et al., 1991). The phosphorylated CFTR channel is gated by ATP binding and hydrolysis (Csanády et al., 2019). The molecular structure of CFTR has been determined in two conformational states (Liu et al., 2017; Zhang et al., 2017, 2018; Zhang and Chen, 2016). In the un-phosphorylated, ATP-free state, the RD lies in between the two NBDs, and the pore is closed(Liu et al., 2017; Zhang and Chen, 2016) . The structure of the phosphorylated, ATP-bound state was obtained from the hydrolysis-deficient mutant E1371Q, which shows that phosphorylation releases the RD from its inhibitory position, permitting NBD dimerization and channel opening (Zhang et al., 2017, 2018).

More than 300 mutations lead to cystic fibrosis, causing various defects in CFTR expression, folding, and channel function (Welsh and Smith, 1993). The most common mutation is the deletion of phenylalanine at position 508 in NBD1 (ΔF508), which results in the retention of folding intermediates in the endoplasmic reticulum (ER) (Cheng et al., 1990). In recent years, CFTR modulators have been developed to revert the effects of the disease-causing mutations (Habib et al., 2019). Small molecules that enhance channel activity are called potentiators, and chemicals that increase the amount of CFTR in the plasmid membrane are called correctors. Currently, one potentiator (ivacaftor) and three correctors (lumacaftor, tezacaftor, and elexacaftor) are in clinical use. Many of the mutations, including ΔF508, cause defects in CFTR biogenesis and channel function. For this reason, most patients require a combination therapy of potentiator and corrector.

Extensive research has been devoted to uncovering the mechanisms of CFTR modulators. Whereas the structural and functional basis of potentiator ivacaftor action has been described (Eckford et al., 2012; Jih and Hwang, 2013; Liu et al., 2019; Van Goor et al., 2009), the mechanism of correctors remains largely undefined. In one study, it was suggested that lumacaftor (formally VX-809) acts through perturbation of membranes, as it appeared to be homogeneously distributed throughout the lipid bilayer (Baroni et al., 2014). In multiple other studies, a direct action on the channel was proposed, but the location of the binding site remains in dispute (Eckford et al., 2014; Farinha and Canato, 2017; He et al., 2013; Hudson et al., 2017; Krainer et al., 2018, 2020; Laselva et al., 2018; Loo et al., 2013; Loo and Clarke, 2017; Okiyoneda et al., 2013; Ren et al., 2013; Sinha et al., 2015).

In this study, we determined cryo-EM structures of lumacaftor-bound CFTR in both the NBD-separated and NBD-dimerized conformations. We also determined the structure of CFTR in complex with tezacaftor (formally VX-661) in the NBD-dimerized

 © 2021 The Author(s). Published by Elsevier Inc.
This is an open access article under the CC BY license (http://creativecommons.org/licenses/by/4.0/).

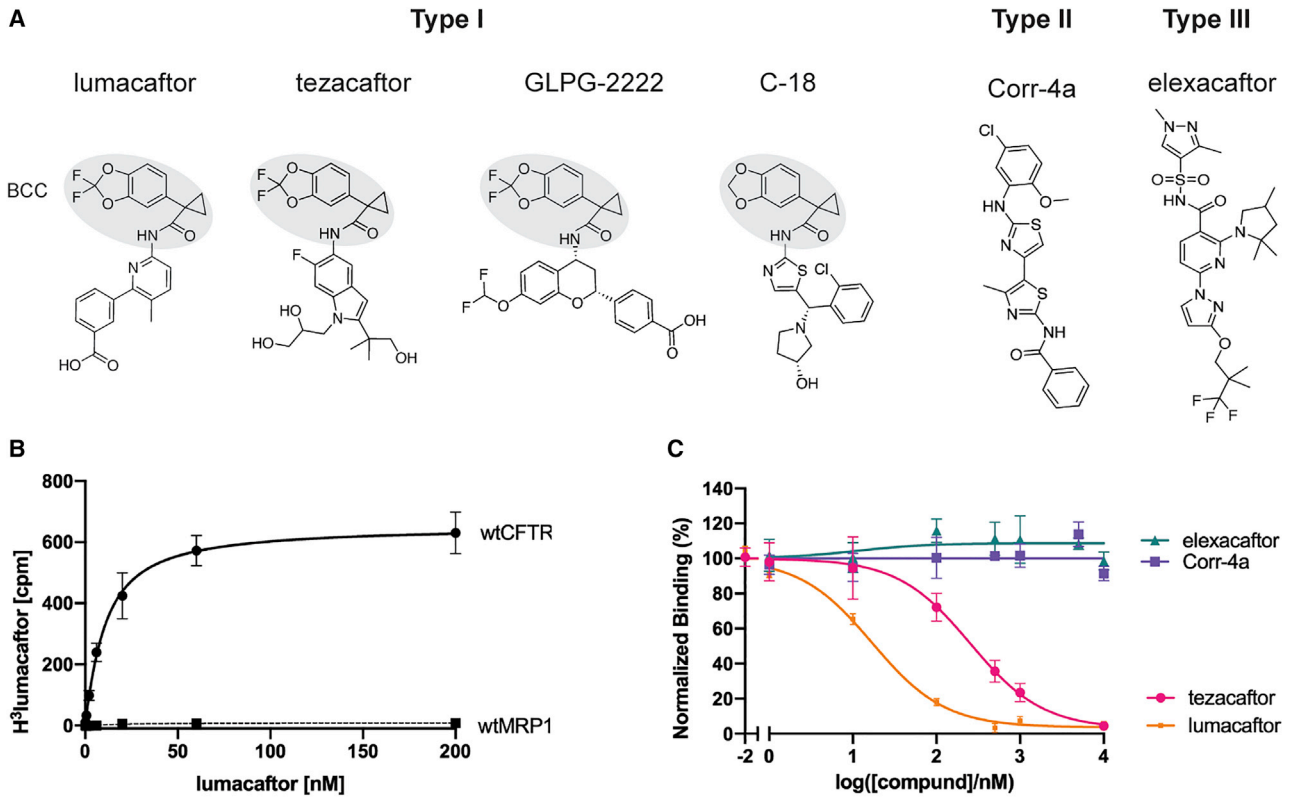

Figure 1. Lumacaftor and tezacaftor bind to CFTR competitively

(A) The chemical structures of representative type I, II and III correctors. The 1,3-**B**enzodioxol-5-yl-**C**yclopropane **C**arboxamide (BCC) headgroup is highlighted in gray.

(B) Saturation binding and nonlinear regression analysis of [^{3}H]lumacaftor binding to *wt*CFTR in the absence of phosphorylation and ATP (K_d = 8.3 ± 2.2 nM). Also shown is a negative control using a related ABC transporter MRP1.

(C) Competition binding assay. The binding of [H^3]lumacaftor (10 nM) was plotted as a function of the competitor's concentration. Data were fit to a single-site competitive binding model. The K_i values for lumacaftor and tezacaftor are 7.7 ± 2.0 nM and 0.12 ± 0.04 mM, respectively. No competition was observed for elexacaftor and Corr-4a. Each data point represents the mean and the standard deviation (SD) of 3–9 of measurements.

conformation. These structures, supported by biochemical and functional data, indicate that these correctors stabilize CFTR by filling an internal cavity on TMD1 and linking together four transmembrane helices that are intrinsically thermodynamically unstable.

RESULTS

Lumacaftor and tezacaftor bind directly to CFTR

CFTR correctors have been categorized into different clusters based on their functional redundancy or additivity. Correctors in the same cluster do not exhibit additive effects and are proposed to share a similar mechanism (Veit et al., 2018, 2020). Correctors from different clusters act through different mechanisms, and some can be combined to synergistically promote CFTR folding (Farinha et al., 2013; Pedemonte et al., 2005; Van Goor et al., 2011; Veit et al., 2018, 2020). Based on this categorization, lumacaftor (VX-809) and tezacaftor (VX-661) belong to the same cluster called type I correctors. They are structural analogs, both containing a 1,3-Benzodioxol-5-yl-Cyclopropane Carboxamide (BCC) headgroup (Figure 1A). Other type I correctors such as C18 (Okiyoneda et al., 2013), ABBV/GLPG-2222 (Wang et al., 2018) (Figure 1A), and ARN23765 (Pedemonte et al., 2020) also share a similar chemical structure and likely a similar mechanism of action.

Although lumacaftor was identified based on its ability to increase cell surface expression of ΔF508-CFTR, its effect is not limited to this particular mutation. Lumacaftor promotes folding of many other mutations as well as the *wt*CFTR (He et al., 2013; Lukacs and Verkman, 2012; Moniz et al., 2013; Ren et al., 2013; Van Goor et al., 2011). A key question to address then is this: does lumacaftor act on misfolded CFTR to restore the tertiary structure, or does it stabilize already-folded CFTR in its native conformation? The latter possibility is supported by two recent studies, which showed that lumacaftor, and its analog C18, bind and stabilize ΔF508-CFTR after its rescue to the cell surface (Eckford et al., 2014; Okiyoneda et al., 2013). C18 also binds directly to purified *wt*CFTR reconstituted in proteoliposomes (Eckford et al., 2014). To measure quantitatively the interactions between lumacaftor and purified *wt*CFTR, we established a scintillation proximity assay (SPA) showing that specific binding of [^{3}H]lumacaftor increases as a function of its

concentration (Figure 1B). The data fit well to a single-site binding model via nonlinear regression analysis, resulting in an equilibrium dissociation constant (K_d) of 8.3 ± 2.2 nM. In comparison, the effective half concentration (EC_{50}) of lumacaftor to rescue ΔF508-CFTR function is reported to be 81 ± 19 nM (Van Goor et al., 2011). The approximate 10-fold difference in the affinity/effective dose is likely explicable on the basis that the former measures the interaction of the drug with *wt*CFTR *in vitro*, whereas the latter measures the cellular effects on the ΔF508 mutant.

To test if lumacaftor and tezacaftor share a common binding site, we performed a competition assay by measuring lumacaftor binding in the presence of increasing concentrations of tezacaftor (Figure 1C). Tezacaftor displaced [^{3}H]lumacaftor in a manner quantitatively consistent with a 1:1 competitive mechanism with an inhibition constant (K_i) equal to 115 ± 42 nM (Figure 1C), also comparable to the potency of tezacaftor in cell-based assays (EC_{50} = 516 nM) (Van Goor et al., 2011; Van Goor et al., 2016, North Amer. Cystic Fibrosis Conference, poster abstract). Using the same competition assay, the K_i of unlabeled lumacaftor was determined to be 7.7 ± 2.0 nM (Figure 1C), consistent with the K_d value determined in the direct binding assay (Figure 1B). Two other structurally unrelated correctors, Corr-4a (type II) and elexacaftor (type III), did not displace [^{3}H]lumacaftor (Figure 1C). The lack of competition by those two correctors is in agreement with folding studies showing that Corr-4a and elexacaftor function synergistically with lumacaftor (Pedemonte et al., 2005; Van Goor et al., 2011; Veit et al., 2020) and do not belong to the type I corrector cluster.

Structural identification of the lumacaftor binding site

To identify the corrector-binding site, we determined the cryo-EM structures of the CFTR/lumacaftor complex in two conformational states (Figures 2A and S1–S3; Table S1). In the absence of phosphorylation and ATP, *wt*CFTR exhibits an NBD-separated conformation as observed before (Liu et al., 2017; Zhang and Chen, 2016). The map, at an overall resolution of 3.9 Å, reveals a ligand density as strong as those of the protein mainchain atoms (Figure S5A). This density is absent from any of the CFTR maps obtained in the absence of a corrector (Figure S3A). The density has an elongated L shape consistent with the chemical structure of lumacaftor (Figure 1A). A higher resolution (2.7 Å) structure was determined from phosphorylated, ATP-bound CFTR (E1371Q), which exhibits the NBD-dimerized conformation as expected (Zhang et al., 2017, 2018). At the same ligand-binding location, we observe a similarly strong but better-defined density that fits lumacaftor unambiguously (Figures 2C–2E and S3A). These results indicate that lumacaftor binds to CFTR in both conformational states.

The binding site is located in TMD1, at the level where the phospholipid head groups of the inner membrane meet the hydrophobic core (Figures 2A and 2B). Lumacaftor interacts with CFTR predominantly through van der Waals interactions, except for a salt bridge with K68 (Figures 2D and 3F). The BCC headgroup, a shared moiety among most type I correctors, inserts into a hydrophobic pocket formed by TM1, 2, 3, and 6 (Figures 2E and 2F). The shape of the BCC headgroup complements the narrow pocket in a classic "key in a lock" fashion (Berg et al., 2019). The polar half of lumacaftor extends outside the pocket, tethering the cytoplasmic ends of TM1 and TM6 together by interacting with residues 70-74 on TM1 and L365 and I368 on TM6 (Figures 2D and 2E).

In agreement with the structure, previous studies showed that the minimal domain sensitive to lumacaftor contains the N-terminal 375 residues (Ren et al., 2013). Removing residues 371-375 rendered lumacaftor ineffectual (Ren et al., 2013). Although residues 371-375 do not contact lumacaftor directly, they interact with N66 and P67, positioning TM1 to coordinate lumacaftor (Figure 2E, cyan ribbon). These observations underscore the structural role of residues 371-375 in constructing the binding site; they also support the previous conclusion that lumacaftor binds to TMD1 in its folded state (Eckford et al., 2014; Okiyoneda et al., 2013).

The location and the chemical nature of lumacaftor-binding are very different from those of the potentiator ivacaftor (Liu et al., 2019). Lumacaftor inserts into a deep pocket in TMD1, and its affinity is mediated through a high degree of shape complementarity, which maximizes van der Waals interactions. In contrast, ivacaftor binds to a shallow cleft on TMD2 at the center of the membrane (Figures 2B and S3A: bottom-right panel, arrow). Mutagenesis studies have shown that hydrogen bonds, rather than van der Waals interactions, play a predominant role in ivacaftor recognition (Liu et al., 2019).

Tezacaftor binds to the same site as lumacaftor

The competition assay data suggested that lumacaftor and tezacaftor share an overlapping binding site on CFTR. To interrogate this conclusion, we determined the structure of tezacaftor-bound CFTR in the NBD-dimerized conformation to 3.8 Å resolution (Figures 3A–3C, S3B, and S4; Table S1). Indeed, a ligand density is observed at the same location in TMD1 (Figures 3B–3E). Inside the hydrophobic pocket, the density also has an elongated shape that fits the BCC headgroup. The density outside the pocket is different than in the lumacaftor-bound structure in a manner consistent with structural differences between the two correctors (Figures 1A, 3B, and 3C).

The BCC headgroup of tezacaftor interacts with the same set of pocket-lining residues as lumacaftor (Figures 3C and 3G). The polar region of tezacaftor, also exposed at the protein/lipid interface, interacts with CFTR in a slightly different manner. Instead of forming a salt bridge with K68, tezacaftor forms an H-bond with R74 (Figures 3C–3G). In addition, tezacaftor interacts with fewer residues in TM1 (Figure 3G), which may explain the relatively lower affinity (Figure 1C) and lower potency of tezacaftor (Van Goor et al., 2011; Van Goor et al., 2016, North Amer. Cystic Fibrosis Conference, poster abstract). Comparison of corrector-bound and -free structures reveals little difference, except for the dispositions of the K68 and R74 side chains (Figure S5). Upon drug binding, the terminal nitrogen on K68 moves about 4 Å to interact with lumacaftor and the side chain of R74 moves 3 Å to interact with either drug.

Binding-site mutations reduce the efficacy of lumacaftor and tezacaftor in rescuing ΔF508-CFTR

Because the structures of drug complexes are of folded CFTR, one might ask whether the structurally identified binding site is

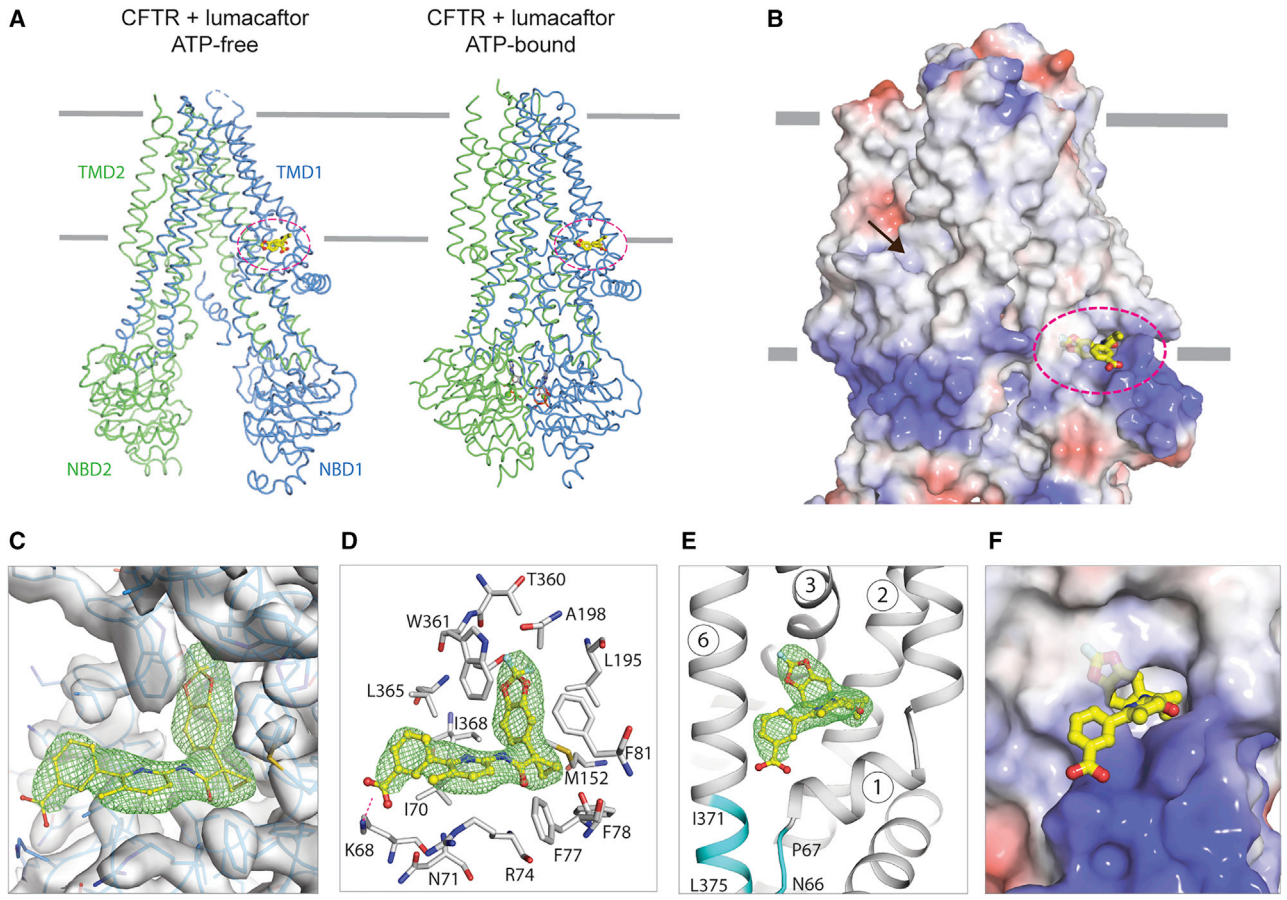

Figure 2. Lumacaftor binds to CFTR in both conformational states

(A) The overall structure of lumacaftor bound to the unphosphorylated, ATP-free *wt*CFTR (left) and phosphorylated, ATP-bound CFTR(E1371Q) (right). TMD1 and NBD1 are shown in blue, TMD2 and NBD2 in green. Lumacaftor is represented in yellow sticks and highlighted by the circle in magenta. The gray lines indicate the membrane boundaries.

(B) Lumacaftor binds at the protein/membrane interface. The surface of the ATP-bound CFTR is shown by electrostatics and scaled from −10kT/e (red) to +10kT/e (blue). For reference, the location of the ivacaftor-binding site is indicated by an arrow.

(C) Experimental density of the lumacaftor-binding site. Protein density is shown in gray and lumacaftor density in green.

(D) Molecular recognition of lumacaftor. Residues within 4.5 Å of lumacaftor are shown as gray sticks. The salt bridge between K68 and lumacaftor is indicated by a magenta dashed line.

(E) The lumacaftor-binding site is formed by TM 1, 2, 3, and 6. Cyan highlights the interactions between residues 371–375 and the N-terminal region of TM1.

(F) Electrostatic surface representation of the same region as in (E).

See also Figures S1, S2, S3, and S5 and Table S1.

the same site of action during CFTR biogenesis. To address this question, we introduced binding site mutations to the ΔF508-CFTR background and analyzed the ability of correctors to rescue these mutants (Figure 4A). Based on the structure, we reason that substituting small pocket-lining residues with larger ones would likely produce steric occlusion of both lumacaftor and tezacaftor. The effects of correctors were quantified using an established gel-shift assay, which measures the abundance of the fully glycosylated CFTR relative to the core-glycosylated form (Figures 4A and S3C). As CFTR exports from the endoplasmic reticulum (ER) to the Golgi apparatus and eventually reaches the plasma membrane, its molecular weight increases due to additional glycosylation (Figure S3C). Lumacaftor and tezacaftor increased the abundance of the mature, fully glycosylated form of the ΔF508 mutant (Figure 4A). This effect is severely diminished by the pocket-lining mutations L195W, A198Y, and S364F (Figure 4A). Furthermore, mutating the three polar residues R74, K68, and N71 generated different responses that are consistent with their structural roles in drug binding (Figure 4A). The R74A substitution lowers the efficacy of both lumacaftor and tezacaftor, consistent with the structures showing that it interacts with both drugs (Figures 2D, 3C, 3D, 3F, and 3G). K68, on the other hand, forms a salt bridge with lumacaftor but makes no contact with tezacaftor (Figures 3D and 3F). Correspondingly, the K68I mutation diminished lumacaftor correction but did not affect tezacaftor. The side chain of N71 projects away from both drugs and its substitution did not affect either corrector (Figures 2D, 3C, and 4A). None of the mutations had a significant effect on the efficacy of elexacaftor/Corr4a, drugs that belong to different classes of correctors (Figure 4A). We

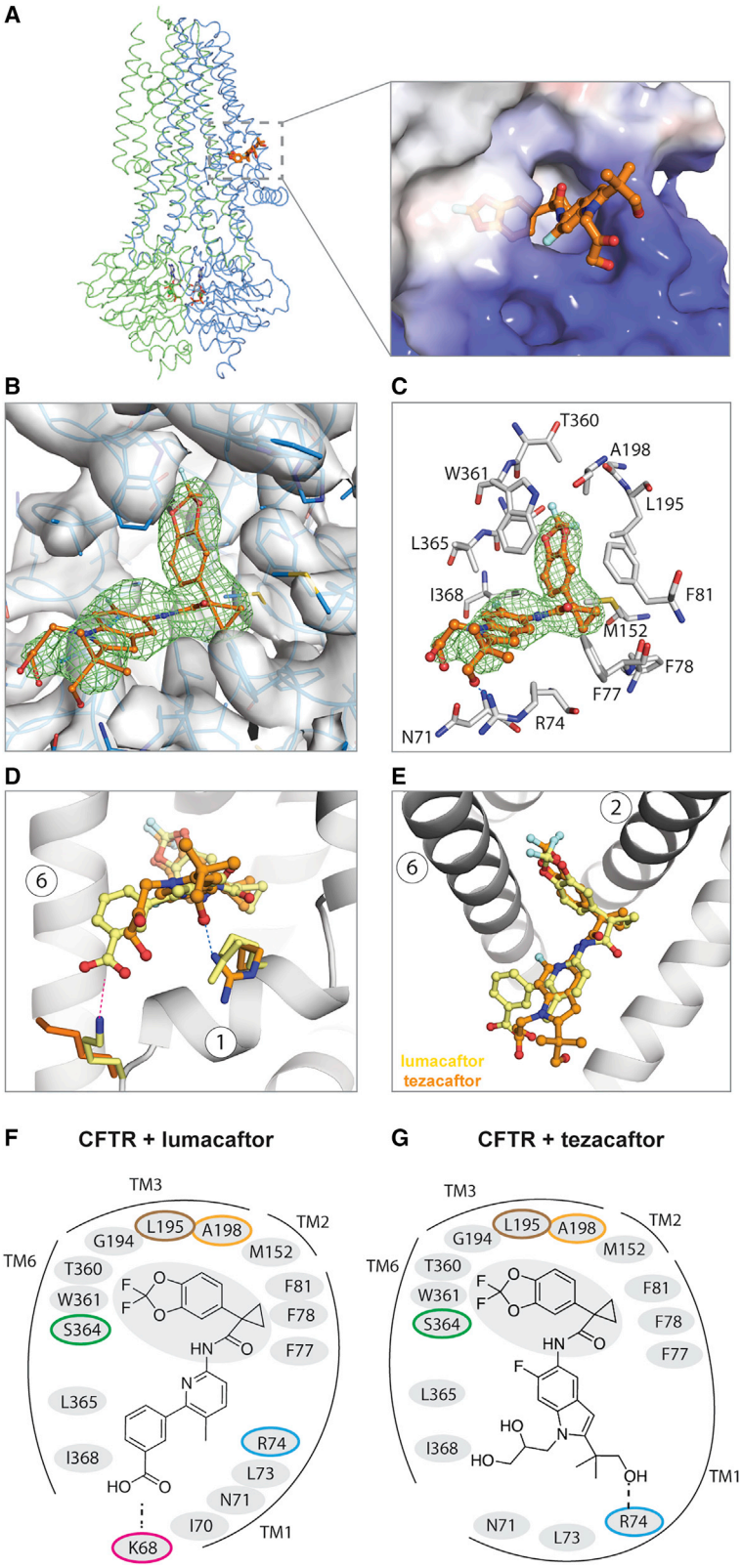

Figure 3. Tezacaftor binds CFTR at the same site as lumacaftor

(A) The overall structure of the CFTR/tezacaftor complex, with a zoomed-in view of the binding site. Tezacaftor is represented in orange sticks, and the protein surface is colored by electrostatics, scaled from −10kT/e (red) to +10kT/e (blue).

(B) Experimental density of the tezacaftor-binding site. Protein density is represented in gray and tezacaftor density in green.

(C) Molecular interaction at the binding site. Restudies within 4.5 Å distance from tezacaftor are shown as gray sticks. The H-bond between R74 and tezacaftor is indicated as a blue dashed line.

(D and E) Two views to compare the structures of lumacaftor (yellow) and tezacaftor (orange). The side chains of K68 and R74 are shown to highlight their different roles in drug binding.

(F and G) Schematic drawing of the CFTR-corrector interactions. All the restudies within 4.5 Å distance of the corrector are depicted. Residues mutated in the maturation and binding assays are indicated with colored circles.

See also Figures S3, S4, and S5 and Table S1.

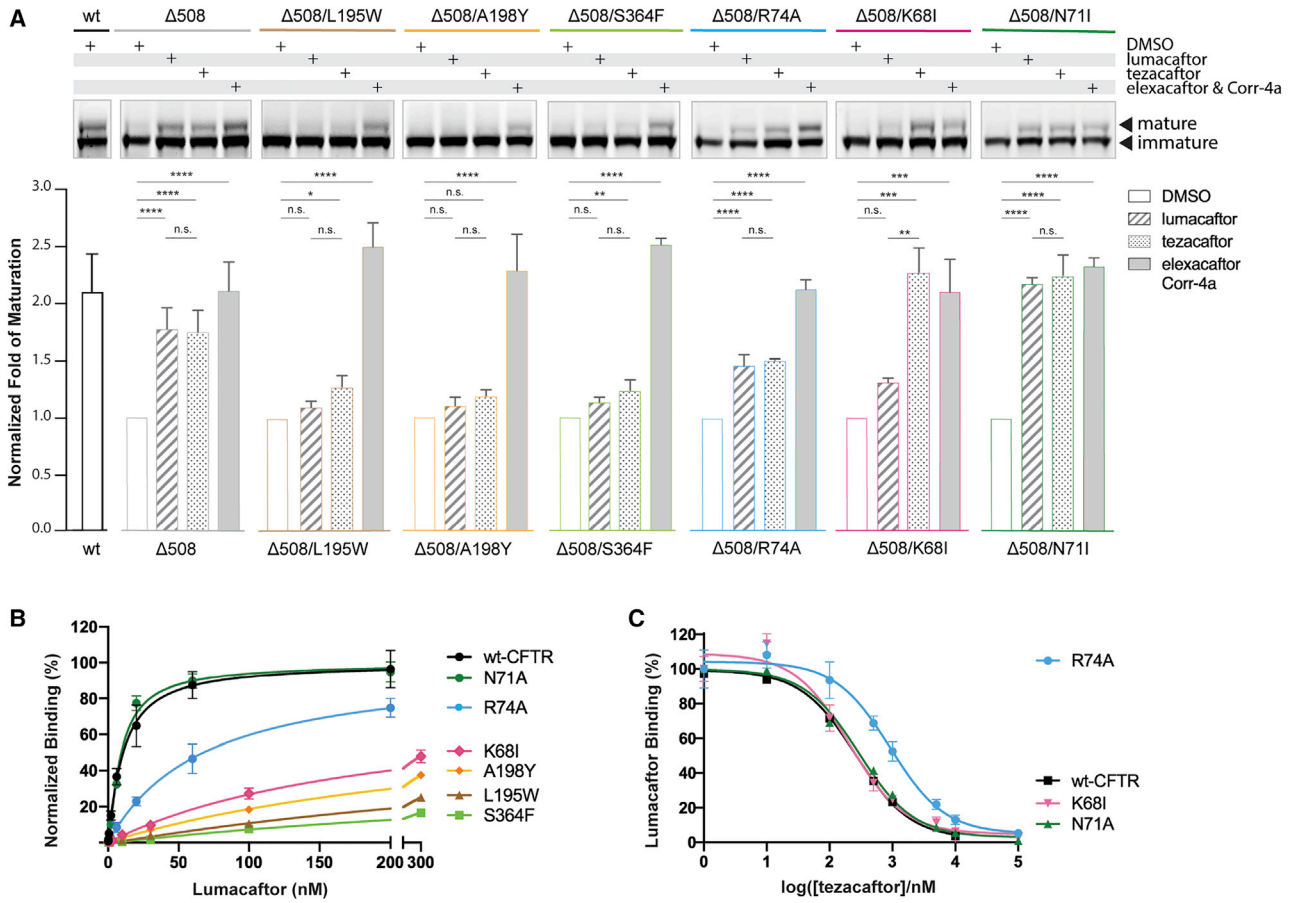

Figure 4. Mutations at the binding site diminished the efficacy of lumacaftor and tezacaftor

(A) Maturation assay of *wt*CFTR, ΔF508-CFTR and binding-site mutations introduced to the ΔF508 background. Upper: SDS-PAGE of cell lysates; both mature and immature CFTR forms were visualized via the C-terminal GFP tag. Lower: Quantification of 3–6 repeats. The standard deviation is indicated as bars. Corrector concentrations: lumacaftor 1 μM, tezacaftor 10 μM, elexacaftor 0.2 μM, Corr-4a 10 μM in 0.1% DMSO. The statistical significance was calculated using the one-way ANOVA. Labels: not significant (n.s.), $p < 0.05$ (*), $p < 0.01$ (**), $p < 0.001$ (***) $p < 0.0001$ (****).

(B) SPA assay to measure the effects of mutations on lumacaftor binding. The K_d values of the polar residue substitutions K68I, R74A, and N71A were 0.19 ± 0.05 mM, 64 ± 13 nM, and 5.9 ± 2.9 nM, respectively. Those of the pocket-lining mutations A198Y, L195W, and S364F were 0.48 ± 0.11 mM, 0.86 ± 0.43 mM, and 1.43 ± 0.74 mM, respectively.

(C) Competition binding assay. The K_i values of K68I, N71A, and R74A CFTR were determined to be 0.12 ± 0.05 mM, 0.13 ± 0.03 mM, and 0.41 ± 0.10 mM, respectively. For reference, the curves of the wtCFTR presented in Figure 1 were also shown (black line). The concentration of [H^3]lumacaftor was kept around the K_d value of the corresponding CFTR construct. Each data point represents the mean and SD of 6–9 of measurements.

See also Figure S3 and Data S1.

also used confocal microscopy to localize CFTR variants in the presence and absence of correctors (Data S1). Consistent with the maturation assay, ΔF508-CFTR is mostly retained in the ER; addition of lumacaftor increased the presence of ΔF508-CFTR at the plasmid membrane. Binding-site mutations L195W, A198Y, S364F, K68I, and R74A, but not the control N71I, specifically reduced the rescuing effects of lumacaftor. Non-type I correctors, on the other hand, were insensitive to the mutations.

To further correlate the functional effects of the direct binding of lumacaftor, we mutated the same residues in the background of *wt*CFTR and measured their affinities for lumacaftor via SPA. The pocket-lining mutations severely reduced lumacaftor binding, likely due to steric-hindrance (Figure 4B). The K68I and R74A reduced the affinities by 23- and 8-fold, respectively (Figure 4B). In contrast, the N71A mutant exhibited an affinity similar to that of the WT protein (Figure 4B). The specificity of these perturbations is further demonstrated in the competition assay, which shows that the binding of tezacaftor is reduced by substitutions of R74, but not K68 nor N71 (Figure 4C). These effects on corrector affinities were not due to defects in folding, as these mutants behaved biochemically similarly to that of WT protein and showed strong binding to ivacaftor, a potentiator that interacts within the TMD2 of CFTR (Baroni et al., 2014; Liu et al., 2019) (Figure S3D).

A recent study showed that lumacaftor does not rescue misfolded zebrafish CFTR (zCFTR) (Laselva et al., 2019) even though its overall structure is very similar to that of human CFTR (Liu

et al., 2017; Zhang and Chen, 2016). Three amino acids distinguish the lumacaftor-binding site in these two CFTR orthologs. A pocket-lining methionine, corresponding to T360 in human CFTR, owing to its larger side chain, likely occludes lumacaftor binding in zCFTR. Furthermore, residues equivalent to K68 and R74 are serine and alanine in zCFTR, respectively. These differences are likely to diminish lumacaftor binding, resulting in its inability to rescue misfolded zCFTR.

DISCUSSION

In this study, we present structures of CFTR in complex with type I correctors lumacaftor and tezacaftor. Consistent with the structure-activity relationship, these two analogous compounds bind to a common site in TMD1. The location of the binding site is entirely consistent with functional studies demonstrating that lumacaftor promotes folding of isolated TMD1 but does not affect other domains (Farinha et al., 2013; Kleizen et al., 2021; Laselva et al., 2018; Loo et al., 2013; Ren et al., 2013). Furthermore, binding of lumacaftor or tezacaftor did not alter the structure of CFTR, supporting the previous conclusion that lumacaftor stabilizes TMD1 in its native conformation (Loo et al., 2013). Binding-site mutations that lowered the affinities of lumacaftor and tezacaftor also diminished their abilities to rescue ΔF508-CFTR, indicating that the structurally identified type I corrector-binding site is the site of action of these drugs to restore CFTR folding.

Earlier work from Braakman and colleagues showed that individual domains of CFTR begin to adopt a tertiary structure as the nascent chain emerges from the ribosome (Kleizen et al., 2005). Folding is completed after the TMDs, NBDs, and R domain assemble into the final structure (Kleizen et al., 2005). The membrane-spanning region of CFTR contains a large number of polar residues, leading to inefficient and slow integration of TM helices in the membrane (Carlson et al., 2005; Hessa et al., 2005; Patrick et al., 2011). In addition, CFTR exhibits a domain-swapped configuration, such that TM helices 1, 2, 3, and 6 pack against TM 10 and 11 to form one bundle; and TM helices 4 and 5 interact with four helices in TMD2 to form another bundle. Such assembly cannot be established until the full-length protein is translated. It is estimated that CFTR synthesis takes about 10 min (Ward and Kopito, 1994), and the subsequent folding and assembly of TMDs and NBDs takes about 30–120 min (Amaral, 2004; Skach, 2006; Wang et al., 2006). During this process, partially folded intermediates linger in the ER, vulnerable to degradation. Consequently, only a small percentage of synthesized CFTR polypeptide reaches the cell surface even for the WT protein (Lukacs et al., 1994; Ward and Kopito, 1994). Folding mutations such as ΔF508 destabilize an individual domain and/or prevent effective interdomain assembly, leading to expansive premature degradation (Cui et al., 2007; Davies et al., 2013; Du and Lukacs, 2009; Lukacs et al., 1994; Rosser et al., 2008; Serohijos et al., 2008; Younger et al., 2006).

The identification of the type I corrector binding site provides a structural basis to understand how these compounds promote CFTR folding. The N-terminal TMD1 is synthesized at an early stage of CFTR biogenesis and folds co-translationally (Kleizen et al., 2005). The four TM helices forming the corrector-binding site are predicted to be unstable. Using an established algorithm (Hessa et al., 2007) to calculate the free energy for membrane insertion ($\Delta G_{insertion}$), we find that TM helices 1, 2, 3, and 6 all have positive values, indicating that these helices individually are unstable in the membrane (Table S2). Instability was also confirmed experimentally for TM6 (Tector and Hartl, 1999). In addition, the tertiary structure formed by TM1, 2, 3, and 6 contains a hydrophobic pocket penetrating into the core of the protein (Figures 2B, 2F, and 3A). Based on the classic work of Matthews, Bowie, and colleagues, the destabilizing energy caused by an internal cavity of this size (360 $Å^3$) is substantial (Eriksson et al., 1992; Joh et al., 2009). Lumacaftor and tezacaftor, with calculated LogP values of 4.96 and 5.52, respectively, have negative ΔG values for membrane partitioning (Liu et al., 2011). Binding of these correctors would structurally link TM 1, 2, 3, and 6 together and contribute to a net negative ΔG for partitioning of the complex. In this manner, the type I correctors are able to stabilize the partially folded TMD1 while it awaits the completion of inter-domain assembly.

Consistent with this analysis, Clarke and colleagues showed that lumacaftor increased the lifetime of TMD1 by about 5-fold (Loo et al., 2013). And most recently, Braakman's laboratory demonstrated that the type I correctors lumacaftor and C18 act at an early folding stage, supporting the hypothesis that rescuing ΔF508 by lumacaftor arises from the increased stability of TMD1 (Kleizen et al., 2021). The same thermodynamic argument also applies to mature CFTR, explaining why the type I correctors can increase the stability of ΔF508 at the plasma membrane (Eckford et al., 2014; Meng et al., 2017).

In summary, the aforementioned structural, theoretical, and experimental data collectively support the following mechanism of action for type I correctors (Figure 5). Once the N-terminal TMD1 is synthesized, it adopts a tertiary structure that is intrinsically unstable in the ER membrane. Binding of lumacaftor or tezacaftor stabilizes TMD1, making it less susceptible to targeted degradation by protein quality control machinery. As CFTR folding is a highly co-operative process, stabilizing TMD1 would ultimately increase the overall probability of forming a fully assembled structure and thereby allosterically rescue many disease-causing mutants that reside in other parts of CFTR. This mechanism is also consistent with the synergy between lumacaftor and suppressor mutations (Farinha et al., 2013; Okiyoneda et al., 2013): lumacaftor extends the lifetime of TMD1 and the suppressor mutations stabilize different parts of CFTR or enhance inter-domain assembly, and thus together they achieve higher rescuing efficiency (Figure 5).

CFTR correctors, discovered empirically, are the most successful drugs to treat diseases caused by defects in protein folding. The proposed mechanism for CFTR correctors provides a conceptual framework to understand how a small molecule can influence protein folding. This concept, rooted in the energetics of protein folding, may also apply to other pharmacological chaperones targeting various misfolded proteins. As of today, most small molecule chaperones were developed as competitive inhibitors binding at the enzymatic active sites (Tran et al., 2020). The disadvantage of this approach is that the drug stabilizes folding of the disease-causing mutants, but

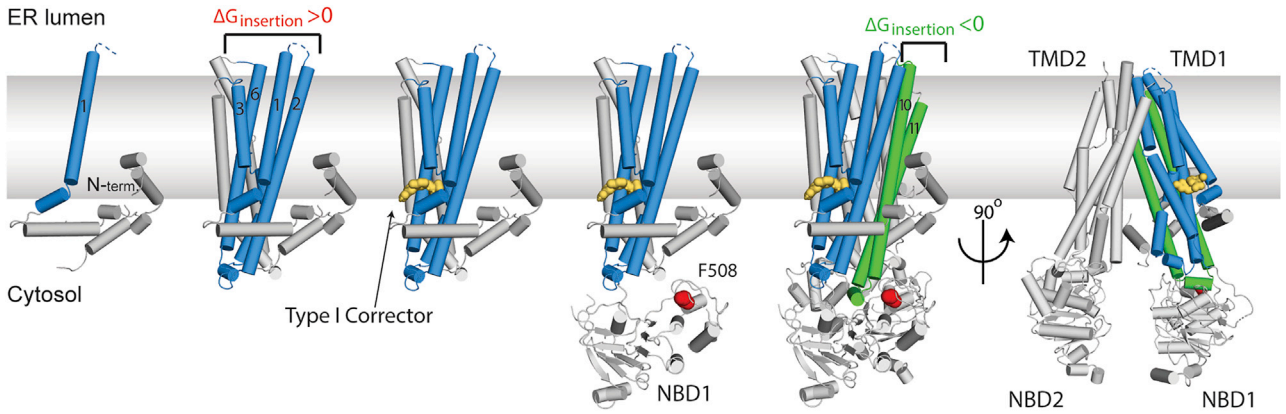

Figure 5. The proposed mechanism of type I correctors

CFTR folds co-translationally as individual domains are synthesized, followed by assembly of the mature tertiary structure. The N-terminal TMD1, synthesized in the early phase, is thermodynamically unstable. The binding of the corrector (yellow sticks) stabilizes TMD1 in the ER membrane, makes it less susceptible to degradation. Increasing the lifetime of TMD1 can partially rescue folding defects in other parts of CFTR, such as ΔF508 in NBD1 (indicated in red). For simplicity, the chaperones that assist CFTR folding are not shown.

See also Table S2.

at the same time, it diminishes enzymatic activity. An alternative approach would be to develop compounds that bind and increase the stability of an individual domain within the target protein. As most proteins fold co-translationally, such compounds can revert folding mutations through an allosteric effect as observed for the CFTR type I correctors.

Limitations of the study

In this study, we identified the binding site of two CFTR drugs lumacaftor and tezacaftor. Based on the structures and thermodynamic principles, we proposed a mechanism of how these molecules improve CFTR folding. Nevertheless, there are limitations associated with the employed techniques. The structures were determined using purified *wt*CFTR instead of disease-related variants such as ΔF508-CFTR. Therefore, the structures do not capture folding defects caused by mutations nor the partially folded structure during CFTR biogenesis. The gel-shift maturation assay reports the relative amounts of glycosylated CFTR, but not the absolute level of rescue efficiency. Lastly, using *in vitro* binding assays, we presented evidence that non-type I correctors do not compete for the same binding site with lumacaftor and tezacaftor; however, this work does not describe the mechanisms of those non-type I correctors. It would be important to understand other types of correctors. Studies of tezacaftor, ivacaftor, and elexacaftor together will collectively reveal the mechanism of the most advanced therapy Trikafta, which is a combination of these three modulators.

STAR★METHODS

Detailed methods are provided in the online version of this paper and include the following:

- KEY RESOURCES TABLE
- RESOURCE AVAILABILITY
  - Lead contact
  - Materials availability
  - Data and code availability
- EXPERIMENTAL MODEL AND SUBJECT DETAILS
  - Cell culture
- METHOD DETAILS
  - Mutagenesis
  - Protein expression and purification
  - EM data acquisition and processing
  - Model building and refinement
  - Maturation assay
  - Scintillation proximity assay
  - Confocal Laser Scanning Microscopy (CLSM) imaging
  - Data Presentation
- QUANTIFICATION AND STATISTICAL ANALYSIS

SUPPLEMENTAL INFORMATION

Supplemental information can be found online at https://doi.org/10.1016/j.cell.2021.12.009.

ACKNOWLEDGMENTS

We thank M. Ebrahim and J. Sotiris at Rockefeller's Evelyn Gruss Lipper Cryo-Electron Microscopy Resource Center for assistance in electron microscopy data collection, F. Glickman of the Rockefeller High-Throughput and Spectroscopy Resource Center for help with the SPA experiments, and P. Banerjee at the Frits and Rita Markus Bio-Imaging Resource Center at The Rockefeller University for assistance in confocal microscopy data collection, Donna Tallent for proofreading the manuscript. We also thank reviewers of Biophysics Colab, R. Gaudet, T.C. Hwang, P. Vergani, and anonymous reviewers of *Cell* for their comments. This work is supported by the Howard Hughes Medical Institute (to J.C.) and the Cystic Fibrosis Foundation Therapeutics (to J.C. and K.F.).

AUTHOR CONTRIBUTIONS

K.F. performed all the experiments. K.F. and J.C. conceptualized the study, analyzed the data, and wrote the manuscript.

DECLARATION OF INTERESTS

The authors declare no competing interests.

Received: May 22, 2021
Revised: October 2, 2021
Accepted: December 9, 2021
Published: January 6, 2022

REFERENCES

Adams, P.D., Afonine, P.V., Bunkóczi, G., Chen, V.B., Davis, I.W., Echols, N., Headd, J.J., Hung, L.W., Kapral, G.J., Grosse-Kunstleve, R.W., et al. (2010). PHENIX: a comprehensive Python-based system for macromolecular structure solution. Acta Crystallogr. D Biol. Crystallogr. *66*, 213–221. https://doi.org/10.1107/S0907444909052925.

Amaral, M.D. (2004). CFTR and chaperones: processing and degradation. J. Mol. Neurosci. *23*, 41–48. https://doi.org/10.1385/JMN:23:1-2:041.

Baroni, D., Zegarra-Moran, O., Svensson, A., and Moran, O. (2014). Direct interaction of a CFTR potentiator and a CFTR corrector with phospholipid bilayers. Eur. Biophys. J. *43*, 341–346. https://doi.org/10.1007/s00249-014-0956-y.

Berg, J.M., Tymoczko, J.L., Gatto, G.J., and Stryer, L. (2019). Biochemistry, Ninth Edition (W.H. Freeman/Macmillan Learning).

Carlson, E., Bays, N., David, L., and Skach, W.R. (2005). Reticulocyte lysate as a model system to study endoplasmic reticulum membrane protein degradation. Methods Mol. Biol. *301*, 185–205. https://doi.org/10.1385/1-59259-895-1:185.

Chen, V.B., Arendall, W.B., 3rd, Headd, J.J., Keedy, D.A., Immormino, R.M., Kapral, G.J., Murray, L.W., Richardson, J.S., and Richardson, D.C. (2010). MolProbity: all-atom structure validation for macromolecular crystallography. Acta Crystallogr. D Biol. Crystallogr. *66*, 12–21. https://doi.org/10.1107/S0907444909042073.

Cheng, S.H., Gregory, R.J., Marshall, J., Paul, S., Souza, D.W., White, G.A., O'Riordan, C.R., and Smith, A.E. (1990). Defective intracellular transport and processing of CFTR is the molecular basis of most cystic fibrosis. Cell *63*, 827–834. https://doi.org/10.1016/0092-8674(90)90148-8.

Cheng, S.H., Rich, D.P., Marshall, J., Gregory, R.J., Welsh, M.J., and Smith, A.E. (1991). Phosphorylation of the R domain by cAMP-dependent protein kinase regulates the CFTR chloride channel. Cell *66*, 1027–1036. https://doi.org/10.1016/0092-8674(91)90446-6.

Csanády, L., Vergani, P., and Gadsby, D.C. (2019). Structure, Gating, and Regulation of the Cftr Anion Channel. Physiol. Rev. *99*, 707–738. https://doi.org/10.1152/physrev.00007.2018.

Cui, L., Aleksandrov, L., Chang, X.B., Hou, Y.X., He, L., Hegedus, T., Gentzsch, M., Aleksandrov, A., Balch, W.E., and Riordan, J.R. (2007). Domain interdependence in the biosynthetic assembly of CFTR. J. Mol. Biol. *365*, 981–994. https://doi.org/10.1016/j.jmb.2006.10.086.

Cutting, G.R. (2015). Cystic fibrosis genetics: from molecular understanding to clinical application. Nat. Rev. Genet. *16*, 45–56. https://doi.org/10.1038/nrg3849.

Davies, J.C., Wainwright, C.E., Canny, G.J., Chilvers, M.A., Howenstine, M.S., Munck, A., Mainz, J.G., Rodriguez, S., Li, H., Yen, K., et al.; VX08-770-103 (ENVISION) Study Group (2013). Efficacy and safety of ivacaftor in patients aged 6 to 11 years with cystic fibrosis with a G551D mutation. Am. J. Respir. Crit. Care Med. *187*, 1219–1225. https://doi.org/10.1164/rccm.201301-0153OC.

Du, K., and Lukacs, G.L. (2009). Cooperative assembly and misfolding of CFTR domains in vivo. Mol. Biol. Cell *20*, 1903–1915. https://doi.org/10.1091/mbc.E08-09-0950.

Eckford, P.D., Li, C., Ramjeesingh, M., and Bear, C.E. (2012). Cystic fibrosis transmembrane conductance regulator (CFTR) potentiator VX-770 (ivacaftor) opens the defective channel gate of mutant CFTR in a phosphorylation-dependent but ATP-independent manner. J. Biol. Chem. *287*, 36639–36649. https://doi.org/10.1074/jbc.M112.393637.

Eckford, P.D., Ramjeesingh, M., Molinski, S., Pasyk, S., Dekkers, J.F., Li, C., Ahmadi, S., Ip, W., Chung, T.E., Du, K., et al. (2014). VX-809 and related corrector compounds exhibit secondary activity stabilizing active F508del-CFTR after its partial rescue to the cell surface. Chem. Biol. *21*, 666–678. https://doi.org/10.1016/j.chembiol.2014.02.021.

Edelheit, O., Hanukoglu, A., and Hanukoglu, I. (2009). Simple and efficient site-directed mutagenesis using two single-primer reactions in parallel to generate mutants for protein structure-function studies. BMC Biotechnol. *9*, 61. https://doi.org/10.1186/1472-6750-9-61.

Emsley, P., and Cowtan, K. (2004). Coot: model-building tools for molecular graphics. Acta Crystallogr. D Biol. Crystallogr. *60*, 2126–2132. https://doi.org/10.1107/S0907444904019158.

Eriksson, A.E., Baase, W.A., Zhang, X.J., Heinz, D.W., Blaber, M., Baldwin, E.P., and Matthews, B.W. (1992). Response of a protein structure to cavity-creating mutations and its relation to the hydrophobic effect. Science *255*, 178–183. https://doi.org/10.1126/science.1553543.

Farinha, C.M., and Canato, S. (2017). From the endoplasmic reticulum to the plasma membrane: mechanisms of CFTR folding and trafficking. Cell. Mol. Life Sci. *74*, 39–55. https://doi.org/10.1007/s00018-016-2387-7.

Farinha, C.M., King-Underwood, J., Sousa, M., Correia, A.R., Henriques, B.J., Roxo-Rosa, M., Da Paula, A.C., Williams, J., Hirst, S., Gomes, C.M., and Amaral, M.D. (2013). Revertants, low temperature, and correctors reveal the mechanism of F508del-CFTR rescue by VX-809 and suggest multiple agents for full correction. Chem. Biol. *20*, 943–955. https://doi.org/10.1016/j.chembiol.2013.06.004.

Goehring, A., Lee, C.H., Wang, K.H., Michel, J.C., Claxton, D.P., Baconguis, I., Althoff, T., Fischer, S., Garcia, K.C., and Gouaux, E. (2014). Screening and large-scale expression of membrane proteins in mammalian cells for structural studies. Nat. Protoc. *9*, 2574–2585. https://doi.org/10.1038/nprot.2014.173.

Habib, A.R., Kajbafzadeh, M., Desai, S., Yang, C.L., Skolnik, K., and Quon, B.S. (2019). A Systematic Review of the Clinical Efficacy and Safety of CFTR Modulators in Cystic Fibrosis. Sci. Rep. *9*, 7234. https://doi.org/10.1038/s41598-019-43652-2.

He, L., Kota, P., Aleksandrov, A.A., Cui, L., Jensen, T., Dokholyan, N.V., and Riordan, J.R. (2013). Correctors of ΔF508 CFTR restore global conformational maturation without thermally stabilizing the mutant protein. FASEB J. *27*, 536–545. https://doi.org/10.1096/fj.12-216119.

Hessa, T., Kim, H., Bihlmaier, K., Lundin, C., Boekel, J., Andersson, H., Nilsson, I., White, S.H., and von Heijne, G. (2005). Recognition of transmembrane helices by the endoplasmic reticulum translocon. Nature *433*, 377–381. https://doi.org/10.1038/nature03216.

Hessa, T., Meindl-Beinker, N.M., Bernsel, A., Kim, H., Sato, Y., Lerch-Bader, M., Nilsson, I., White, S.H., and von Heijne, G. (2007). Molecular code for transmembrane-helix recognition by the Sec61 translocon. Nature *450*, 1026–1030. https://doi.org/10.1038/nature06387.

Hudson, R.P., Dawson, J.E., Chong, P.A., Yang, Z., Millen, L., Thomas, P.J., Brouillette, C.G., and Forman-Kay, J.D. (2017). Direct Binding of the Corrector VX-809 to Human CFTR NBD1: Evidence of an Allosteric Coupling between the Binding Site and the NBD1:CL4 Interface. Mol. Pharmacol. *92*, 124–135. https://doi.org/10.1124/mol.117.108373.

Jih, K.Y., and Hwang, T.C. (2013). Vx-770 potentiates CFTR function by promoting decoupling between the gating cycle and ATP hydrolysis cycle. Proc. Natl. Acad. Sci. USA *110*, 4404–4409. https://doi.org/10.1073/pnas.1215982110.

Joh, N.H., Oberai, A., Yang, D., Whitelegge, J.P., and Bowie, J.U. (2009). Similar energetic contributions of packing in the core of membrane and water-soluble proteins. J. Am. Chem. Soc. *131*, 10846–10847. https://doi.org/10.1021/ja904711k.

Johnson, Z.L., and Chen, J. (2017). Structural Basis of Substrate Recognition by the Multidrug Resistance Protein MRP1. Cell *168*, 1075–1085. https://doi.org/10.1016/j.cell.2017.01.041.

Kleizen, B., van Vlijmen, T., de Jonge, H.R., and Braakman, I. (2005). Folding of CFTR is predominantly cotranslational. Mol. Cell *20*, 277–287. https://doi.org/10.1016/j.molcel.2005.09.007.

Kleizen, B., van Willigen, M., Mijnders, M., Peters, F., Grudniewska, M., Hillenaar, T., Thomas, A., Kooijman, L., Peters, K.W., Frizzell, R., et al. (2021). Co--translational folding of the first transmembrane domain of ABC-transporter CFTR is supported by assembly with the first cytosolic domain. J. Mol. Biol. *433*, 166955. Published online December 20, 2020. https://doi.org/10.1101/2020.12.19.423590.

Krainer, G., Treff, A., Hartmann, A., Stone, T.A., Schenkel, M., Keller, S., Deber, C.M., and Schlierf, M. (2018). A minimal helical-hairpin motif provides molecular-level insights into misfolding and pharmacological rescue of CFTR. Commun Biol *1*, 154. https://doi.org/10.1038/s42003-018-0153-0.

Krainer, G., Schenkel, M., Hartmann, A., Ravamehr-Lake, D., Deber, C.M., and Schlierf, M. (2020). CFTR transmembrane segments are impaired in their conformational adaptability by a pathogenic loop mutation and dynamically stabilized by Lumacaftor. J. Biol. Chem. *295*, 1985–1991. https://doi.org/10.1074/jbc.AC119.011360.

Laselva, O., Marzaro, G., Vaccarin, C., Lampronti, I., Tamanini, A., Lippi, G., Gambari, R., Cabrini, G., Bear, C.E., Chilin, A., and Dechecchi, M.C. (2018). Molecular Mechanism of Action of Trimethylangelicin Derivatives as CFTR Modulators. Front. Pharmacol. *9*, 719. https://doi.org/10.3389/fphar.2018.00719.

Laselva, O., Erwood, S., Du, K., Ivakine, Z., and Bear, C.E. (2019). Activity of lumacaftor is not conserved in zebrafish Cftr bearing the major cystic fibrosis-causing mutation. FASEB Bioadv *1*, 661–670. https://doi.org/10.1096/fba.2019-00039.

Liu, X., Testa, B., and Fahr, A. (2011). Lipophilicity and its relationship with passive drug permeation. Pharm. Res. *28*, 962–977. https://doi.org/10.1007/s11095-010-0303-7.

Liu, F., Zhang, Z., Csanady, L., Gadsby, D.C., and Chen, J. (2017). Molecular Structure of the Human CFTR Ion Channel. Cell *169*, 85–95. https://doi.org/10.1016/j.cell.2017.02.024.

Liu, F., Zhang, Z., Levit, A., Levring, J., Touhara, K.K., Shoichet, B.K., and Chen, J. (2019). Structural identification of a hotspot on CFTR for potentiation. Science *364*, 1184–1188. https://doi.org/10.1126/science.aaw7611.

Loo, T.W., and Clarke, D.M. (2017). Corrector VX-809 promotes interactions between cytoplasmic loop one and the first nucleotide-binding domain of CFTR. Biochem. Pharmacol. *136*, 24–31. https://doi.org/10.1016/j.bcp.2017.03.020.

Loo, T.W., Bartlett, M.C., and Clarke, D.M. (2013). Corrector VX-809 stabilizes the first transmembrane domain of CFTR. Biochem. Pharmacol. *86*, 612–619. https://doi.org/10.1016/j.bcp.2013.06.028.

Lukacs, G.L., and Verkman, A.S. (2012). CFTR: folding, misfolding and correcting the ΔF508 conformational defect. Trends Mol. Med. *18*, 81–91. https://doi.org/10.1016/j.molmed.2011.10.003.

Lukacs, G.L., Mohamed, A., Kartner, N., Chang, X.B., Riordan, J.R., and Grinstein, S. (1994). Conformational maturation of CFTR but not its mutant counterpart (delta F508) occurs in the endoplasmic reticulum and requires ATP. EMBO J. *13*, 6076–6086.

Meng, X., Wang, Y., Wang, X., Wrennall, J.A., Rimington, T.L., Li, H., Cai, Z., Ford, R.C., and Sheppard, D.N. (2017). Two Small Molecules Restore Stability to a Subpopulation of the Cystic Fibrosis Transmembrane Conductance Regulator with the Predominant Disease-causing Mutation. J. Biol. Chem. *292*, 3706–3719. https://doi.org/10.1074/jbc.M116.751537.

Moniz, S., Sousa, M., Moraes, B.J., Mendes, A.I., Palma, M., Barreto, C., Fragata, J.I., Amaral, M.D., and Matos, P. (2013). HGF stimulation of Rac1 signaling enhances pharmacological correction of the most prevalent cystic fibrosis mutant F508del-CFTR. ACS Chem. Biol. *8*, 432–442. https://doi.org/10.1021/cb300484r.

Moriarty, N.W., Grosse-Kunstleve, R.W., and Adams, P.D. (2009). electronic Ligand Builder and Optimization Workbench (eLBOW): a tool for ligand coordinate and restraint generation. Acta Crystallogr. D Biol. Crystallogr. *65*, 1074–1080. https://doi.org/10.1107/S0907444909029436.

Okiyoneda, T., Veit, G., Dekkers, J.F., Bagdany, M., Soya, N., Xu, H., Roldan, A., Verkman, A.S., Kurth, M., Simon, A., et al. (2013). Mechanism-based corrector combination restores ΔF508-CFTR folding and function. Nat. Chem. Biol. *9*, 444–454. https://doi.org/10.1038/nchembio.1253.

Patrick, A.E., Karamyshev, A.L., Millen, L., and Thomas, P.J. (2011). Alteration of CFTR transmembrane span integration by disease-causing mutations. Mol. Biol. Cell *22*, 4461–4471. https://doi.org/10.1091/mbc.E11-05-0396.

Pedemonte, N., Lukacs, G.L., Du, K., Caci, E., Zegarra-Moran, O., Galietta, L.J., and Verkman, A.S. (2005). Small-molecule correctors of defective DeltaF508-CFTR cellular processing identified by high-throughput screening. J. Clin. Invest. *115*, 2564–2571. https://doi.org/10.1172/JCI24898.

Pedemonte, N., Bertozzi, F., Caci, E., Sorana, F., Di Fruscia, P., Tomati, V., Ferrera, L., Rodriguez-Gimeno, A., Berti, F., Pesce, E., et al. (2020). Discovery of a picomolar potency pharmacological corrector of the mutant CFTR chloride channel. Sci Adv *6*, eaay9669. https://doi.org/10.1126/sciadv.aay9669.

Pettersen, E.F., Goddard, T.D., Huang, C.C., Couch, G.S., Greenblatt, D.M., Meng, E.C., and Ferrin, T.E. (2004). UCSF Chimera–a visualization system for exploratory research and analysis. J. Comput. Chem. *25*, 1605–1612. https://doi.org/10.1002/jcc.20084.

Ren, H.Y., Grove, D.E., De La Rosa, O., Houck, S.A., Sopha, P., Van Goor, F., Hoffman, B.J., and Cyr, D.M. (2013). VX-809 corrects folding defects in cystic fibrosis transmembrane conductance regulator protein through action on membrane-spanning domain 1. Mol. Biol. Cell *24*, 3016–3024. https://doi.org/10.1091/mbc.E13-05-0240.

Rohou, A., and Grigorieff, N. (2015). CTFFIND4: Fast and accurate defocus estimation from electron micrographs. J. Struct. Biol. *192*, 216–221. https://doi.org/10.1016/j.jsb.2015.08.008.

Rosser, M.F., Grove, D.E., Chen, L., and Cyr, D.M. (2008). Assembly and misassembly of cystic fibrosis transmembrane conductance regulator: folding defects caused by deletion of F508 occur before and after the calnexin-dependent association of membrane spanning domain (MSD) 1 and MSD2. Mol. Biol. Cell *19*, 4570–4579. https://doi.org/10.1091/mbc.E08-04-0357.

Scheres, S.H. (2012). RELION: implementation of a Bayesian approach to cryo-EM structure determination. J. Struct. Biol. *180*, 519–530. https://doi.org/10.1016/j.jsb.2012.09.006.

Schindelin, J., Arganda-Carreras, I., Frise, E., Kaynig, V., Longair, M., Pietzsch, T., Preibisch, S., Rueden, C., Saalfeld, S., Schmid, B., et al. (2012). Fiji: an open-source platform for biological-image analysis. Nat. Methods *9*, 676–682. https://doi.org/10.1038/nmeth.2019.

Serohijos, A.W., Hegedus, T., Aleksandrov, A.A., He, L., Cui, L., Dokholyan, N.V., and Riordan, J.R. (2008). Phenylalanine-508 mediates a cytoplasmic-membrane domain contact in the CFTR 3D structure crucial to assembly and channel function. Proc. Natl. Acad. Sci. USA *105*, 3256–3261. https://doi.org/10.1073/pnas.0800254105.

Shaikh, T.R., Gao, H., Baxter, W.T., Asturias, F.J., Boisset, N., Leith, A., and Frank, J. (2008). SPIDER image processing for single-particle reconstruction of biological macromolecules from electron micrographs. Nat. Protoc. *3*, 1941–1974. https://doi.org/10.1038/nprot.2008.156.

Sinha, C., Zhang, W., Moon, C.S., Actis, M., Yarlagadda, S., Arora, K., Woodroofe, K., Clancy, J.P., Lin, S., Ziady, A.G., et al. (2015). Capturing the Direct Binding of CFTR Correctors to CFTR by Using Click Chemistry. ChemBioChem *16*, 2017–2022. https://doi.org/10.1002/cbic.201500123.

Skach, W.R. (2006). CFTR: new members join the fold. Cell *127*, 673–675. https://doi.org/10.1016/j.cell.2006.11.002.

Tector, M., and Hartl, F.U. (1999). An unstable transmembrane segment in the cystic fibrosis transmembrane conductance regulator. EMBO J. *18*, 6290–6298. https://doi.org/10.1093/emboj/18.22.6290.

Tran, M.L., Génisson, Y., Ballereau, S., and Dehoux, C. (2020). Second-Generation Pharmacological Chaperones: Beyond Inhibitors. Molecules *25*, E3145. https://doi.org/10.3390/molecules25143145.

Van Goor, F., Hadida, S., Grootenhuis, P.D., Burton, B., Cao, D., Neuberger, T., Turnbull, A., Singh, A., Joubran, J., Hazlewood, A., et al. (2009). Rescue of CF airway epithelial cell function in vitro by a CFTR potentiator, VX-770. Proc. Natl. Acad. Sci. USA *106*, 18825–18830. https://doi.org/10.1073/pnas.0904709106.

Van Goor, F., Hadida, S., Grootenhuis, P.D., Burton, B., Stack, J.H., Straley, K.S., Decker, C.J., Miller, M., McCartney, J., Olson, E.R., et al. (2011). Correction of the F508del-CFTR protein processing defect in vitro by the investigational drug VX-809. Proc. Natl. Acad. Sci. USA *108*, 18843–18848. https://doi.org/10.1073/pnas.1105787108.

Veit, G., Xu, H., Dreano, E., Avramescu, R.G., Bagdany, M., Beitel, L.K., Roldan, A., Hancock, M.A., Lay, C., Li, W., et al. (2018). Structure-guided combination therapy to potently improve the function of mutant CFTRs. Nat. Med. *24*, 1732–1742. https://doi.org/10.1038/s41591-018-0200-x.

Veit, G., Roldan, A., Hancock, M.A., Da Fonte, D.F., Xu, H., Hussein, M., Frenkiel, S., Matouk, E., Velkov, T., and Lukacs, G.L. (2020). Allosteric folding correction of F508del and rare CFTR mutants by elexacaftor-tezacaftor-ivacaftor (Trikafta) combination. JCI Insight *5*, 139983. https://doi.org/10.1172/jci.insight.139983.

Wang, X., Venable, J., LaPointe, P., Hutt, D.M., Koulov, A.V., Coppinger, J., Gurkan, C., Kellner, W., Matteson, J., Plutner, H., et al. (2006). Hsp90 cochaperone Aha1 downregulation rescues misfolding of CFTR in cystic fibrosis. Cell *127*, 803–815. https://doi.org/10.1016/j.cell.2006.09.043.

Wang, X., Liu, B., Searle, X., Yeung, C., Bogdan, A., Greszler, S., Singh, A., Fan, Y., Swensen, A.M., Vortherms, T., et al. (2018). Discovery of 4-[(2R,4R)-4-({[1-(2,2-Difluoro-1,3-benzodioxol-5-yl)cyclopropyl]carbonyl}amino)- 7-(difluoromethoxy)-3,4-dihydro-2H-chromen-2-yl]benzoic Acid (ABBV/GLPG-2222), a Potent Cystic Fibrosis Transmembrane Conductance Regulator (CFTR) Corrector for the Treatment of Cystic Fibrosis. J. Med. Chem. *61*, 1436–1449. https://doi.org/10.1021/acs.jmedchem.7b01339.

Ward, C.L., and Kopito, R.R. (1994). Intracellular turnover of cystic fibrosis transmembrane conductance regulator. Inefficient processing and rapid degradation of wild-type and mutant proteins. J. Biol. Chem. *269*, 25710–25718.

Welsh, M.J., and Smith, A.E. (1993). Molecular mechanisms of CFTR chloride channel dysfunction in cystic fibrosis. Cell *73*, 1251–1254. https://doi.org/10.1016/0092-8674(93)90353-r.

Younger, J.M., Chen, L., Ren, H.Y., Rosser, M.F., Turnbull, E.L., Fan, C.Y., Patterson, C., and Cyr, D.M. (2006). Sequential quality-control checkpoints triage misfolded cystic fibrosis transmembrane conductance regulator. Cell *126*, 571–582. https://doi.org/10.1016/j.cell.2006.06.041.

Zhang, K. (2016). Gctf: Real-time CTF determination and correction. J. Struct. Biol. *193*, 1–12. https://doi.org/10.1016/j.jsb.2015.11.003.

Zhang, Z., and Chen, J. (2016). Atomic Structure of the Cystic Fibrosis Transmembrane Conductance Regulator. Cell *167*, 1586–1597. https://doi.org/10.1016/j.cell.2016.11.014.

Zhang, Z., Liu, F., and Chen, J. (2017). Conformational Changes of CFTR upon Phosphorylation and ATP Binding. Cell *170*, 483–491. https://doi.org/10.1016/j.cell.2017.06.041.

Zhang, Z., Liu, F., and Chen, J. (2018). Molecular structure of the ATP-bound, phosphorylated human CFTR. Proc. Natl. Acad. Sci. USA *115*, 12757–12762. https://doi.org/10.1073/pnas.1815287115.

Zheng, S.Q., Palovcak, E., Armache, J.P., Verba, K.A., Cheng, Y., and Agard, D.A. (2017). MotionCor2: anisotropic correction of beam-induced motion for improved cryo-electron microscopy. Nat. Methods *14*, 331–332. https://doi.org/10.1038/nmeth.4193.

STAR★METHODS

KEY RESOURCES TABLE

REAGENT or RESOURCE	SOURCE	IDENTIFIER
Chemicals, peptides, and recombinant proteins		
2,2-didecylpropane-1,3-bis-b-D-maltopyranoside (LMNG)	Anatrace	NG310
Cholesteryl hemisuccinate (CHS)	Anatrace	CH210
Digitonin	Sigma-Aldrich	D141
sf-900 II SFM medium	GIBCO	Cat#10902-088
Cellfectin II reagents	Invitrogen	Cat#10362-100
Lipofectamine 3000	Invitrogen	Cat #: L3000008
Freestyle 293 medium	GIBCO	Cat#12338-018
GlutaMAX	GIBCO	Cat# 35050079
DMEM-F12 medium	ATCC	Cat#30-2006
PKA catalytic subunit, recombinant	NEB	Cat#P6000L
ATP	Sigma-Aldrich	A2383
Lambda Protein Phosphatase (Lambda PP)	NEB	Cat#P0753L
Alexa Fluor 647- conjugated wheat germ agglutinin	ThermoFisher	Cat#W32466
Lumacaftor	MCE	Cat#HY-13262
Tezacaftor	MCE	Cat#HY-15448
Elexacaftor	Selleckchem	Cat#2FE4A758
Corr4a	Fisher	Cat#421580-53-2
Lumacaftor [H3]	Moravek	N/A
Critical commercial assays		
CNBR-activated Sepharose beads	GE Healthcare	17-0430-01
Superose 6, 10/300 GL	GE Healthcare	17-5172-01
Deposited data		
Coordinates of phosphorylated, lumacaftor and ATP bound CFTR	This paper	PDB: 7SVD
Cryo-EM map of phosphorylated, lumacaftor and ATP bound CFTR	This paper	EMD-25447
Coordinates of phosphorylated, tezacaftor and ATP bound CFTR	This paper	PDB: 7SV7
Cryo-EM map of phosphorylated, tezacaftor and ATP bound CFTR	This paper	EMD-25445
Coordinates of dephosphorylated, lumacaftor bound CFTR	This paper	PDB: 7SVR
Cryo-EM map of dephosphorylated, lumacaftor bound CFTR	This paper	EMD-25452
Dephosphorylated, ATP-free human cystic fibrosis transmembrane conductance regulator (CFTR)	Liu et al., 2017	PDB: 5UAK
Complex of human cystic fibrosis transmembrane conductance regulator (CFTR) and GLPG1837	(Liu et al., 2019)	PDB: 6O1V
Experimental models: Cell lines		
Sf9	ATCC	CRL-1711
CHO-K1	ATCC	CCL-61
HEK293S GnTI-	ATCC	CRL-3022

(*Continued on next page*)

Continued		
REAGENT or RESOURCE	SOURCE	IDENTIFIER
Oligonucleotides		
See Table S3 for list of nucleotides used in this study		N/A
Recombinant DNA		
Human CFTR cloned onto a modified pEG Bacmam vector suitable for expression in mammalian cells	This paper	N/A
Bovine MRP1 cloned onto a modified pEG Bacmam vector suitable for expression in mammalian cells	This paper	N/A
Software and algorithms		
Imspector	Aberrior	https://imspector.abberior-instruments.com/
MotionCorr2	(Zheng et al., 2017)	https://emcore.ucsf.edu/ucsf-software
GCTF	Zhang, 2016	https://www2.mrc-lmb.cam.ac.uk/research/locally-developed-software/zhang-software/
CTFFIND4	Rohou and Grigorieff, 2015	http://grigoriefflab.janelia.org/ctffind4
Gautomatch	Zhang K.	https://www2.mrc-lmb.cam.ac.uk/research/locally-developed-software/zhang-software/
RELION 3.1	Scheres, 2012	http://www2.mrc-lmb.cam.ac.uk/relion
COOT	(Emsley and Cowtan, 2004)	https://www2.mrc-lmb.cam.ac.uk/personal/pemsley/coot
DG prediction	Hessa et al., 2007	https://dgpred.cbr.su.se/results.php?program=TMpred
PHENIX	Adams et al., 2010	https://www.phenix-online.org
eLBOW	(Moriarty et al., 2009)	eLBOW
MolProbity	Chen et al., 2010	http://molprobity.biochem.duke.edu
BFACTOR.EXE	Grigorieff N.	https://grigoriefflab.janelia.org/bfactor
Other		
R1.2/1.3 400 mesh Au holey carbon grids	Quantifoil	Cat#1210627

RESOURCE AVAILABILITY

Lead contact

Requests regarding reagents and further information may be addressed to the lead contact, Jue Chen (juechen@rockefeller.edu).

Materials availability

This study did not generate new unique reagents.

Data and code availability

- All generated maps and models have been deposited to PDB/EMDataBank and are publicly available as of the date of publication. IDs are listed in the key resources table.
- Any additional information required to reanalyze the data reported in this paper is available from the lead contact upon request.
- This paper does not report original code.

EXPERIMENTAL MODEL AND SUBJECT DETAILS

Cell culture

Sf9 cells were cultured in Sf-900 II SFM medium (GIBCO) supplemented with 5% FBS and 1% Antibiotic-Antimycotic. HEK293S GnTI$^-$ cells were cultured in Freestyle 293 (GIBCO) supplemented with 2% FBS and 1% Antibiotic-Antimycotic. HEK293F cells were cultured in DMEM F-12 (ATCC) supplemented with 10% FBS and 1% Antibiotic-Antimycotic. CHO K-1 cells were cultured in DMEM F-12 supplemented with 10% FBS and 1X GlutaMAX (GIBCO).

METHOD DETAILS

Mutagenesis

All mutations were introduced using the SPRINP mutagenesis methodology (Table S3) (Edelheit et al., 2009). Mutagenesis primers were designed to be complementary, be of 15-45 nt length and contain the mutated bases close to the center. The parental plasmid containing CFTR cDNA was amplified in two separated reactions congaing either forward or reverse primer. Next, two single-primer PCR products were combined, denatured (95°C, 5 min.) and cooled gradually over 5 min. to 37°C. The sample was digested for 12 hr. in 37°C. 3 mL of the digest was added to 50 mL of competent XL1-Blue cells for transformation. The cell suspension was spread on LB/ampicillin plates. After incubating the plates overnight at 37°C random colonies were picked and expanded. Purified plasmid DNA (QIAGEN Plasmid Kit) was sent for sequencing (Genewiz).

Protein expression and purification

All CFTR constructs were expressed and purified as described (Goehring et al., 2014; Zhang and Chen, 2016). Briefly, bacmids carrying CFTR constructs were generated in E. Coli DH10Bac cells (Invitrogen). Recombinant baculoviruses were produced and amplified in Sf9 cells. Proteins were expressed in HEK293S GnTI$^-$ cells infected with 10% baculovirus at a density of 2.7x10^6 cells/mL. Cells were induced with 10 mM sodium butyrate 12 hours after infection and cultured at 30°C for another 48 hours before harvesting. Proteins for cryo-EM studies were purified as the following. Cells were solubilized in buffer containing 1.2% 2,2- didecylpropane-1,3-bis-b-D-maltopyranoside (LMNG) and 0.24% Cholesteryl hemisuccinate (CHS). Protein was purified via its C-terminal green fluorescence protein (GFP) tag using GFP nanobody coupled Sepharose Beads (GE Healthcare) and eluted by removing the GFP tag with the PreScission Protease. The wild-type sample was de-phosphorylated using l-phosphatase. The CFTR (E1371Q) sample was phosphorylated with protein kinase A. At the final step, protein samples were purified on size exclusion chromatography in 0.06% (*wt*CFTR/lumacaftor and CFTR (E1371Q)/tezacaftor samples) or 0.03% (CFTR (E1371Q)/lumacaftor) digitonin. Samples for SPA assays were purified using the same protocol except that they were not treated with Protein Kinase A nor l-phosphatase.

EM data acquisition and processing

Immediately after size exclusion chromatography, the CFTR (E1371Q) sample (at 5 mg/mL) was incubated with 10 mM ATP, 8 mM $MgCl_2$ and 200 μM lumacaftor or tezacaftor on ice for 30 min. The *wt*CFTR sample (5mg/mL; 32 μM) was incubated with 200 μM lumacaftor. About 3 mM fluorinated Fos-choline-8 was added to the samples right before freezing on to Quantifoil R1.2/1.3 400 mesh Au grids using Vitrobot Mark IV (FEI).

Cryo-EM images were collected on a 300 kV Titian Krios (FEI) with a K2 or K3 Summit detector (Gatan) using SerialEM (Table S1). The images were corrected for gain reference and binned by 2. Drift correction was performed using MotionCorr (Zheng et al., 2017). Contrast transfer function (CTF) estimation was performed using CTFFIND4 (Rohou and Grigorieff, 2015) and GCTF (Zhang, 2016). Based on CTFFIND4 results, all the images at resolution lower than 5Å were removed. For further processing steps, GCTF generated values were used. Particles were automatically picked by Gautomatch (https://www.mrc-lmb.cam.ac.uk/kzhang/) for the *wt*CFTR/lumacaftor and CFTR(E1371Q)/tezacaftor datasets. For the CFTR (E1371Q)/lumacaftor data, picking was performed using RELION implemented Laplacian-of-Gaussian blob detection. All the subsequent steps of maps reconstruction and resolution estimations were performed using RELION 3.1(Scheres, 2012) (Figure S1, S2, S4).

Each dataset processing was optimized individually to obtain the best results. In general, after the first 3D classification, the 3D refinement was performed and followed by a second run of 3D classification without particles orientation optimization. However, in the case of the tezacaftor dataset, using reference model filtered to different resolutions (8 Å, 25 Å or 60 Å) gave similar quality maps but of different particles distribution. After visual inspection, the best quality classes from each run were combined and particle duplicates were removed. The resulting set of particles was refined to a higher resolution than any of the sets from individual 3D classifications. The combined particle set was polished, 3D refined, and 3D classified again against a model at 25 Å resolution. For the two lumacaftor datasets, changing the resolution of the reference model did not make significant difference (Figure S1, S2, S4).

Model building and refinement

The initial protein models were built by fitting the published CFTR structures (PDB:5UAK and 6O1V) into the cryo-EM maps using UCSF Chimera (Pettersen et al., 2004). In the *wt*CFTR/lumacaftor structure, the sidechains of the NBDs were trimmed due to the limited resolution of ~4.5 Å (Figure S1). Models were then adjusted based on the cryo-EM densities using Coot (Emsley and Cowtan, 2004). Lumacaftor and tezacaftor were built into the drug density and refined in PHENIX (Adams et al., 2010) using restrains generated by eLBOW (Moriarty et al., 2009). MolProbity (Chen et al., 2010) was used for geometries validation.

Model overfitting was assessed as described (Johnson and Chen, 2017). Each model refined against half-map 1, converted to an electron density map using UCSF Chimera, and SPIDER (Shaikh et al., 2008) was used to calculate FSC plots between the converted

map and the full map, the half-map 1, and the half-map 2. The cryo-EM maps were masked with a generous mask about 3.5 times larger than the volume of the model density. The FSC plots were then corrected for the volume by which the mask exceeds the volume of the model density using Equation 1:

$$FSC_{corrected} = \frac{f * FSC}{1 + (f - 1) * FSC} \quad (1)$$

Where f is equal to the factor by which the mask exceeds the volume of the model density (Figure S1, S2, S4).

Maturation assay

HEK293F cells grown in a 6-well plate were transiently transfected with CFTR constructs labeled with C-terminal eGFP tag using Lipofectamine 3000 (ThermoFisher) in Opti-MEM (GIBCO) medium. Cells were incubated with DNA/transfection mixture for 12 hours at 37°C, then in DMEM F-12 supplemented with 10 mM sodium butyrate and the corrector of choice at 30°C for another 24 hours. Cells were harvested by re-suspending in 1 mL ice-cold PBS and spun down in 1.5 mL tubes for 5 min. at 5,000 rpm, 4°C.

Cell pellets were re-suspended in buffer containing 1.2% 2,2- didecylpropane-1,3-bis-b-D-maltopyranoside (LMNG) and 0.24% Cholesteryl hemisuccinate (CHS) and rotated for 60 min. at 4°C. Cell lysates were spun down for 60 min. at 45,000 rpm, supernatants were analyzed on a 4%–20% gradient tris-glycine SDS-PAGE gel (ThermoFisher). Gels were imaged to visualize the GFP signal, which was quantified using Fiji (Schindelin et al., 2012). The background signal was subtracted from the CFTR bands. The proportion of mature CFTR to total CFTR ($k_{m/t}$) was calculated using Equation 2 and then normalized to that of the DMSO treated sample. The statistical significance was calculated using the one-way ANOVA method implemented in GraphPad Prism 8 (GraphPad Software, San Diego, California, USA, https://www.graphpad.com).

$$k_{m/t} = \frac{CFTR_{mature}}{(CFTR_{mature} + CFTR_{immature})} \quad (2)$$

Scintillation proximity assay

The binding and competition assays were performed as described (Liu et al., 2019). CFTR constructs used in this assay contain a C-terminal Strep-tag, followed by a PreScission Protease cleavage site, and a GFP tag. The GFP tag was removed during purification whereas the Strep-tag was retained to attach CFTR to the SPA beads. To measure lumacaftor binding, 5 nM CFTR was incubated with 0.5 mg/mL YSi streptavidin SPA beads (PerkinElmer) in the presence of varying concentrations of lumacaftor (at 1:1 molar ratio of cold and [^{3}H] lumacaftor (6.4 Ci/mmol, synthesized by Moravek) in buffer containing 20 mM Tris-HCl pH 7.5, 200 mM NaCl, 0.06% digitonin, 2 mM DTT and 0.1% Tween 20 at 4°C for 1 hr. The reactions were carried out in 96-well non-binding surface microplates (Corning) and data were recorded using a Microbeta Trilux plate reader (PerkinElmer). Specific binding was obtained by subtracting background radioligand binding in the absence of protein. The K_d values were calculated by fitting the data with a single-site saturation binding model accounting for ligand depletion using GraphPad Prism 8. The K_i values of tezacaftor were calculated by fitting the data with a single-site competitive binding model in GraphPad Prism 8. The readings were normalized by dividing the specific binding with the total binding (Bmax) and represented in percentages.

Confocal Laser Scanning Microscopy (CLSM) imaging

CHO cells were seeded in Ibidi μ-Slide 4 Well Ph+ chambered coverslips and cultured in CHO media. After 24 hours at 37°C, cell media was exchanged for OpitMEM and cells were transiently transfected with mCherry tagged Tapasin and eGFP tagged CFTR isoforms using Lipofectamine 3000 according to manufacturer's instructions. About 12 hours after transfection, the media was exchanged back to CHO cell media supplemented with 10 mM sodium butyrate and selected drug (lumacaftor at 1 μM, tezacaftor at 10 μM or elexacaftor at 0.2 μM and Corr4a at 10 μM cocktail). DMSO (0.1%) were included in all samples. Next, cells were incubated at 30°C for 24 hours and then were fixed with 2% paraformaldehyde (15 min at room temperature), stained with Alexa Fluor 647- conjugated wheat germ agglutinin (15 min at room temperature), and mounted with glycerol/n-propyl gallate. Imaging was performed using the Abberior Facility Line STED/confocal system with a 100X/1.40 NA oil objective (Olympus UPLSAPO100XO objective, oil r.i. 1.518 at 23°C) on an Olympus IX83 stand, pulsed 405 / 485 / 561 / 640 nm excitation laser lines, and spectral detection setup with single-photon-counting avalanche photodiode (APD) detectors. Pixel sizes and z-steps were computed to satisfy Nyquist criteria. Images were acquired as .obf file format using Abberior Imspector software, which automatically adjusted the detection bands (eGFP:498-551nm, mCherry:571-630nm, Alexa Fluor 647:650-760nm) and the confocal pinhole (1 A.U) based on selected wavelengths. Care was taken to avoid pixel saturation and bleaching by optimizing laser power, accumulation and pixel dwell times, while trying to collect an optimal number of photons. Acquisition parameters were kept constant between images. Post-acquisition, images were further processed and analyzed in Fiji.

Data Presentation

Structural figures were generated using UCSF Chimera, PyMOL and Fiji. Plots were generated using GraphPad Prism8. Particles Euler angle histograms were generated using *plot_indiveuler_histogram_fromstarfile.py* script (https://github.com/leschzinerlab/Relion). All the figures were assembled using Adobe Illustrator.

QUANTIFICATION AND STATISTICAL ANALYSIS

The quantification and statistical analyses are integral parts of the software and algorithms used. Details are described in the main text and methods sections.

CellPress
OPEN ACCESS

Supplemental figures

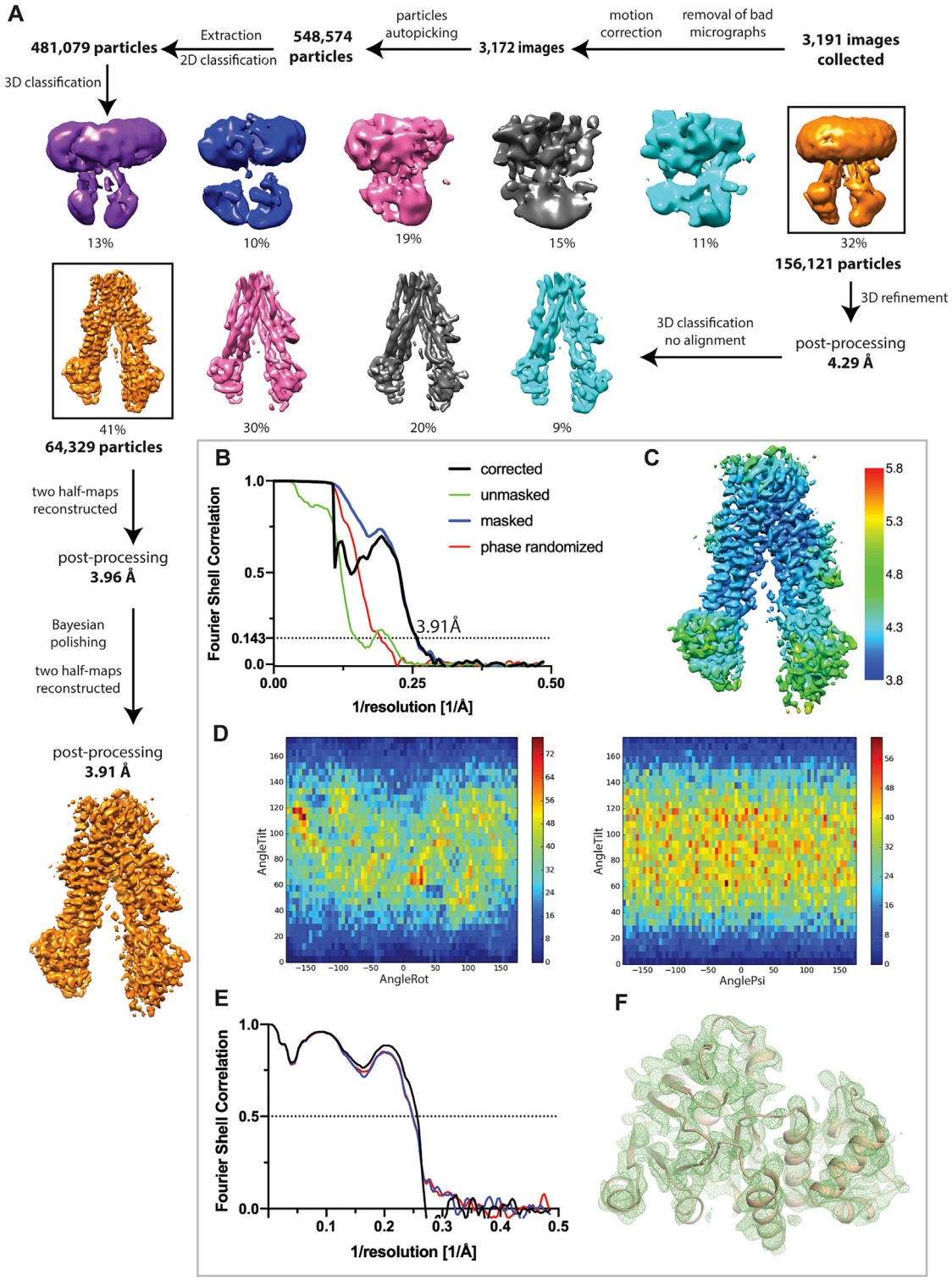

Figure S1. Cryo-EM analysis of the CFTR/lumacaftor complex and quality of the reconstruction, related to Figure 2

(A) Image processing procedure. (B) Fourier shell correlation curves of the final map. (C) Local resolution estimation of the final map. (D) Particles orientation distribution histograms. (E) Model-to-map fit for the full map (black), half-map 1 (blue), half-map 2 (red). (F) EM density of NBD2.

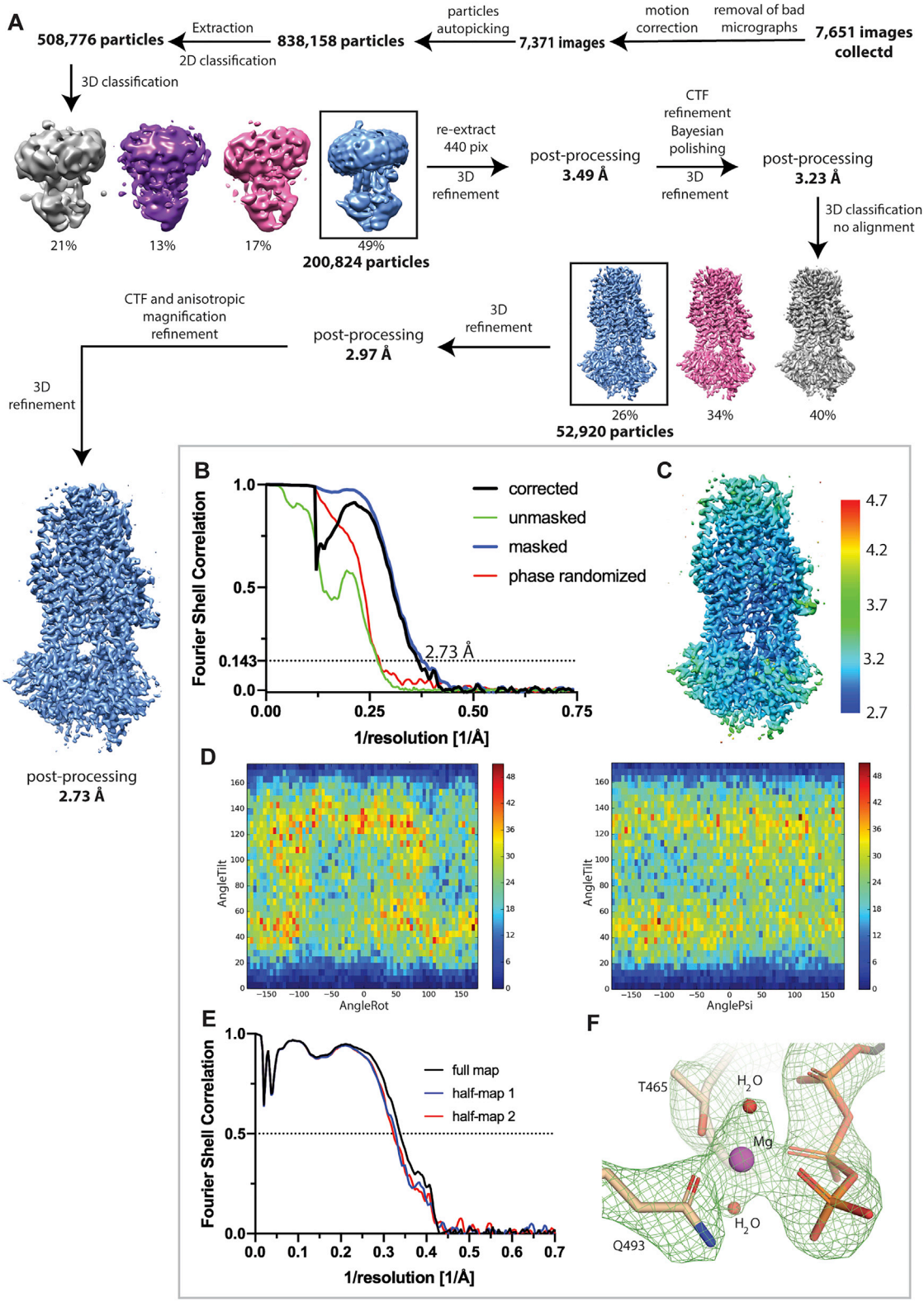

Figure S2. Cryo-EM analysis of the CFTR/lumacaftor/ATP complex and quality of the reconstruction, related to Figure 2

(A) Image processing procedure. (B) Fourier shell correlation curves of the final map. (C) Local resolution estimation of the final map. (D) Particles orientation distribution histograms. (E) Model-to-map fit for the full map (black), half-map 1 (blue), half-map 2 (red). (F) EM density at the degenerate ATP binding site.

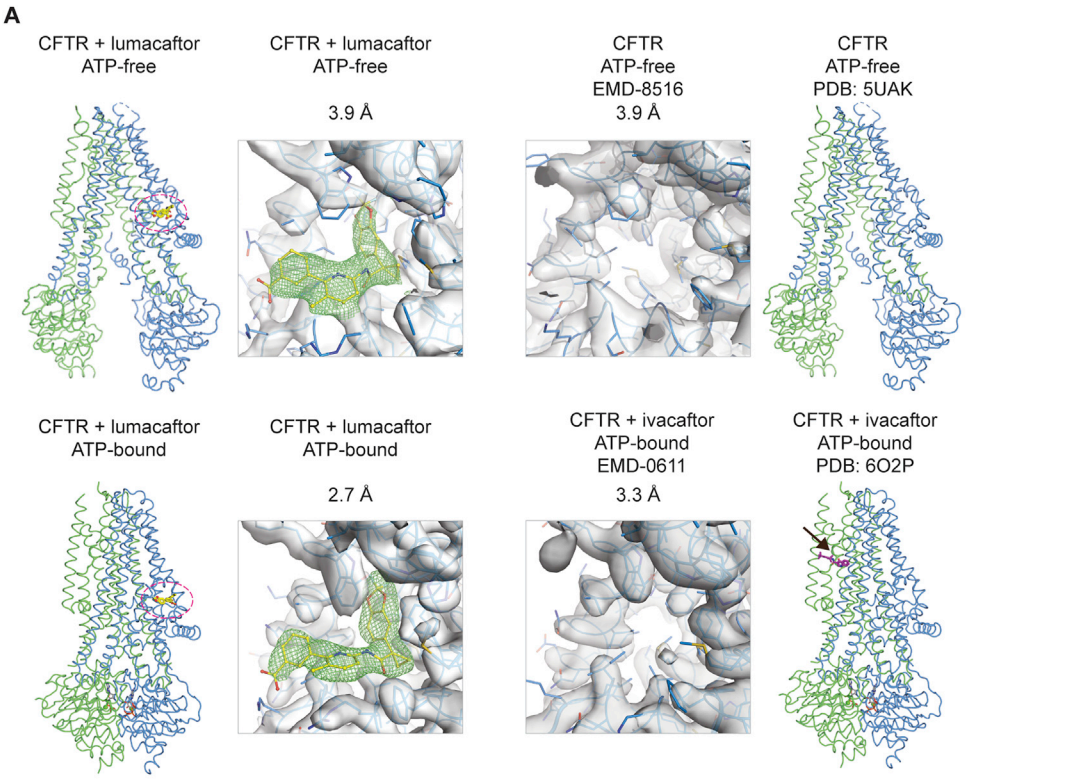

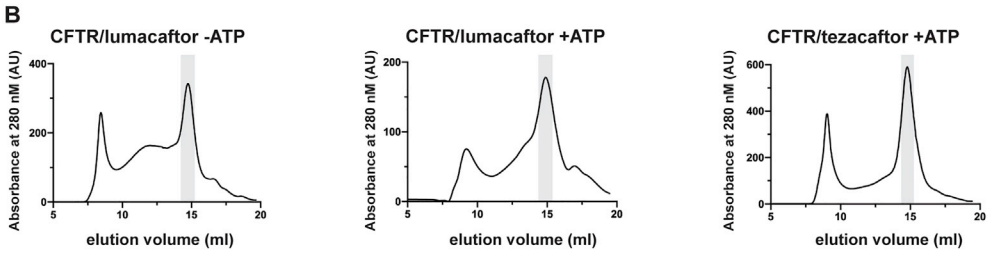

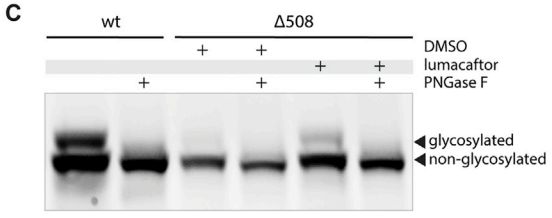

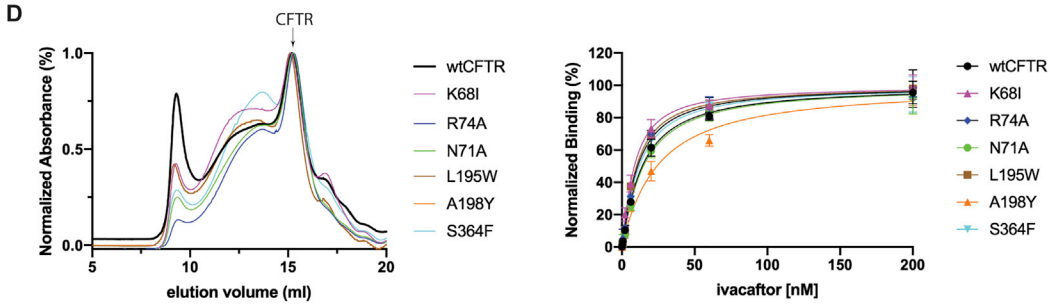

(legend on next page)

Figure S3. Comparison of the EM density at the corrector-binding site and assessment of folding, stability, and maturation of the constructs used in the study, related to Figures 2, 3, and 4

(A) The lumacaftor-bound, NBD-separated structure (this study, upper-left panel). The apo structure (PDB:5UAK and EMD-8516, upper-right panel). The lumacaftor-bound, NBD-dimerized structure (this study, lower-left). The ivacaftor-bound structure (PDB:6O2P and EMD-0611, lower-right panel), the black arrow indicates binding site of the potentiator ivacaftor (magenta sticks). All maps were contoured to show similar density for the CFTR main chain and side chains. (B) Purification of CFTR for cryo-EM experiments. Size exclusion chromatography profiles of the wt (left panel) and E1371Q (middle and right panels) CFTR. The elution volumes of monomeric CFTR fractions used for grids preparation are shaded in gray. (C) Test of sensitivity of the mature, glycosylated form of CFTR to PNGase F treatment. (D) Size exclusion chromatography profiles of the wt and mutant CFTR (upper panel). The position of monomeric CFTR is indicated by an arrow. Quantitative measurement of CFTR-ivacaftor interactions (lower panel). The Kd values of the wt, K68I, R74A, N71A, L195W, A198Y and S364F CFTR were calculated to be 11.4 ± 2.5 nM, 6.1 ± 2.0 nM, 8.2 ± 2.0 nM, 12.1 ± 3.9 nM, 7.3 ± 2.6 nM, 21.9 ± 8.6 nM and 9.0 ± 2.6 nM respectively.

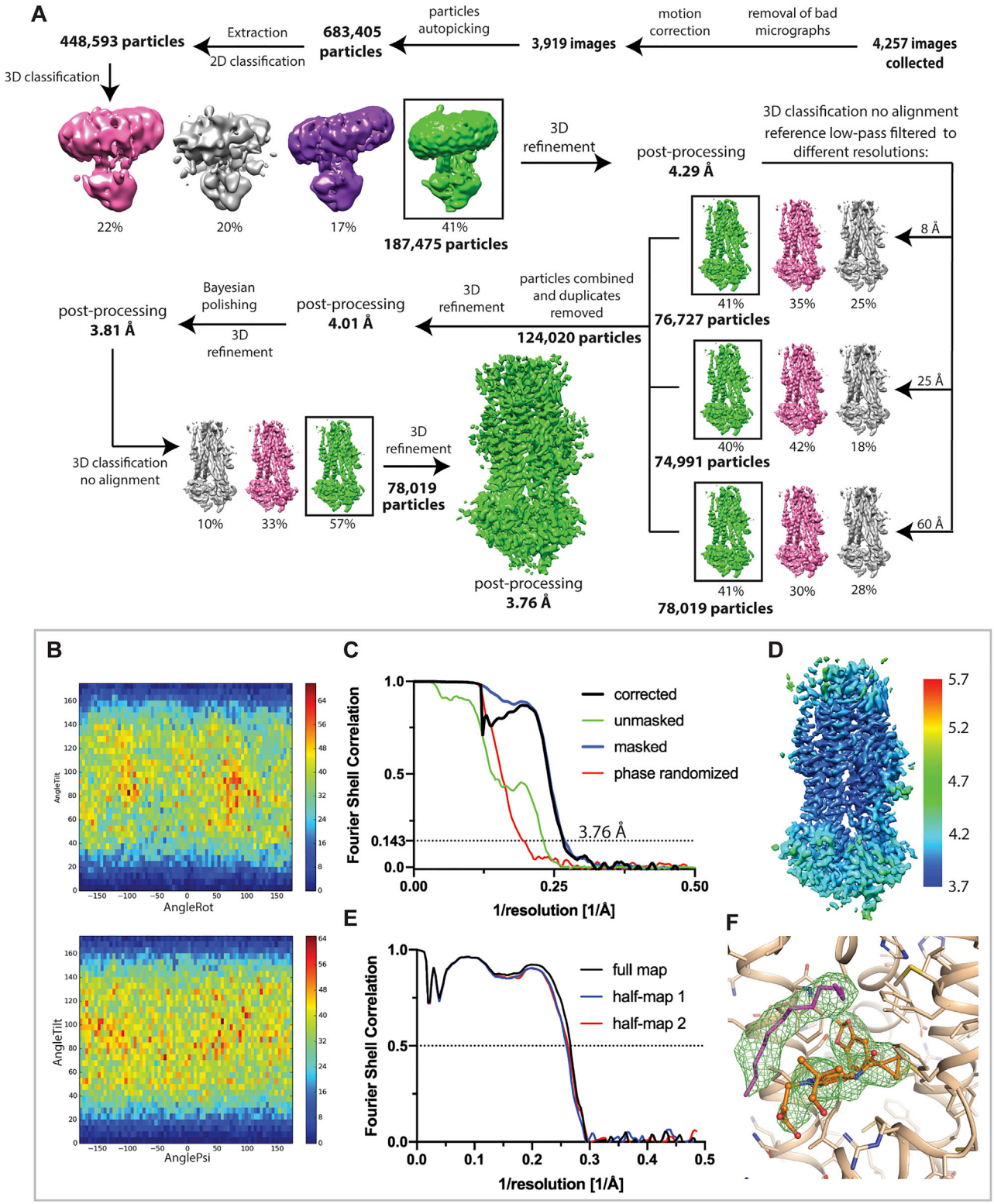

Figure S4. Cryo-EM analysis of the CFTR/tezacaftor/ATP complex and quality of the reconstruction, related to Figure 3

(A) Image processing procedure. (B) Particles orientation distribution histograms. (C) Fourier shell correlation curves of the final map. (D) Local resolution estimation of the final map. (E) Model-to-map fit for the full map (black), half-map 1 (blue), half-map 2 (red). (F) EM density at the tezacaftor-binding site. The lipid acyl chain is represented as magenta sticks.

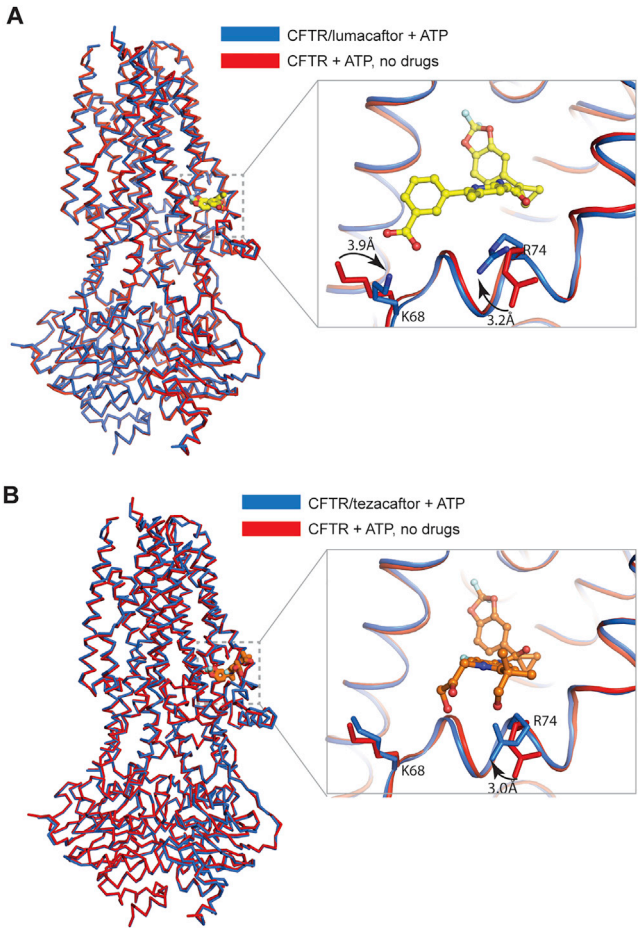

Figure S5. Comparison of the corrector-bound and drug-free CFTR structures, related to Figures 2 and 3

(A) Superposition of the CFTR/lumacaftor (blue) and drug-free (red) (PDB:6MSM) structures. Inset: local rearrangements of sidechains at the lumacaftor-binding site. Lumacaftor is represented in yellow sticks. (B) Superposition of the CFTR/tezacaftor (blue) and drug-free (red)(PDB:6MSM) structures. Inset: local rearrangements of sidechains the tezacaftor-binding site. Tezacaftor is represented in orange sticks.